

## Article

# Optimizing Oxygen Electrode Bifunctionality with Platinum and Nickel Nanoparticle-Decorated Nitrogen-Doped Binary Metal Oxides

Dušan Mladenović <sup>1</sup> , Yasemin Aykut <sup>2</sup>, Ayşe B. Yurtcan <sup>2</sup> , Gulin S. P. Soylu <sup>3</sup> , Diogo M. F. Santos <sup>4</sup> ,  
Šćepan Miljanić <sup>1</sup> and Biljana Šljukić <sup>1,4,\*</sup> 

<sup>1</sup> University of Belgrade, Faculty of Physical Chemistry, Studentski Trg 12-16, 11158 Belgrade, Serbia; dusan.mladenovic@ffh.bg.ac.rs (D.M.); epan@ffh.bg.ac.rs (Š.M.)

<sup>2</sup> Department of Chemical Engineering, Atatürk University, Erzurum 25240, Turkey; yaseminn.aykut@gmail.com (Y.A.); abayrakceken@atauni.edu.tr (A.B.Y.)

<sup>3</sup> Chemical Engineering Department, Faculty of Engineering, Istanbul University-Cerrahpasa, Avcilar, Istanbul 34320, Turkey; gpozan@iuc.edu.tr

<sup>4</sup> Center of Physics and Engineering of Advanced Materials, Laboratory for Physics of Materials and Emerging Technologies, Chemical Engineering Department, Instituto Superior Técnico, Universidade de Lisboa, 1049-001 Lisbon, Portugal; diogosantos@tecnico.ulisboa.pt

\* Correspondence: biljana.paunkovic@tecnico.ulisboa.pt

**Abstract:** Developing bifunctional oxygen electrode materials with superior activity for oxygen reduction (ORR) and oxygen evolution (OER) reactions is essential for advancing regenerative fuel cell and rechargeable metal–air battery technologies. This present work deals with the synthesis and characterization of electrocatalysts containing Pt and Ni nanoparticles supported on nitrogen-doped mixed metal oxides (Mn<sub>2</sub>O<sub>3</sub>-NiO) and the systematic evaluation of their bifunctional ORR/OER performance in an alkaline medium. These electrocatalysts have been successfully synthesized by a simple and fast microwave method. PtNi/Mn<sub>2</sub>O<sub>3</sub>-NiO-N with a binary metal oxide-to-N ratio of 1:2 demonstrated the best performance among the studied materials regarding bifunctional electrocatalytic activity ( $\Delta E = 0.96$  V) and robust stability.

**Keywords:** oxygen reduction reaction; oxygen evolution reaction; bifunctional electrocatalyst; binary metal oxides; platinum and nickel nanoparticles



**Citation:** Mladenović, D.; Aykut, Y.; Yurtcan, A.B.; Soylu, G.S.P.; Santos, D.M.F.; Miljanić, Š.; Šljukić, B. Optimizing Oxygen Electrode Bifunctionality with Platinum and Nickel Nanoparticle-Decorated Nitrogen-Doped Binary Metal Oxides. *Processes* **2024**, *12*, 453. <https://doi.org/10.3390/pr12030453>

Academic Editor: Jia Huo

Received: 2 February 2024

Revised: 16 February 2024

Accepted: 18 February 2024

Published: 23 February 2024



**Copyright:** © 2024 by the authors. Licensee MDPI, Basel, Switzerland. This article is an open access article distributed under the terms and conditions of the Creative Commons Attribution (CC BY) license (<https://creativecommons.org/licenses/by/4.0/>).

## 1. Introduction

In light of the increased energy demand in the 21st century, there is a global need to find alternative power sources to replace fossil fuels in the years to come. Global reserves of fossil fuels are limited, and some predictions state they will be entirely depleted by the year 2050 to 2070 [1]. Furthermore, burning fossil fuels emits a vast amount of greenhouse gases into the atmosphere, dramatically impacting climate change. Decreasing carbon emissions is one of the main goals to minimize or possibly reverse climate change. Therefore, scientists worldwide have devoted themselves to discovering and optimizing new long-term solutions for providing humankind with the power it needs in the future. As mentioned, next-generation power sources should be eco-friendly and cheap, implement renewable energy sources as the primary energy source, and be paired with devices that can convert and store the produced energy when there is an increased inflow from the primary source. On the other hand, those devices should be capable of converting the stored energy back to electricity when the primary source is unavailable.

One potential bifunctional device is an electrochemical device called regenerative fuel cells. These devices can operate in discrete or unitized modes [2]. Discrete regenerative fuel cells combine two separate units: a fuel cell and an electrolyzer. In contrast, unitized regenerative fuel cells use one pair of electrodes that can intermittently operate

in two modes: fuel cell mode (FC-mode), in which the device produces electricity from chemical reactants (fuel and oxidant); and electrolysis mode (El-mode), where the device produces the reactants when there is an inflow of electrical energy. Suppose such a device is constructed, and its construction is relatively simple and cheap, it may be implemented in the hydrogen economy concept, one of the most promising energy concepts for the future [3–5]. To construct a unitized regenerative alkaline fuel cell (URAFc), one must first solve the problem of the oxygen side of such a cell [6,7]. Namely, two reactions occur on the oxygen side of URAFCs: the oxygen reduction reaction (ORR) in FC-mode and the oxygen evolution reaction (OER) in El-mode. Both reactions have sluggish kinetics and, thus, represent the performance-limiting factors in many systems [8,9].

Platinum (Pt) is currently considered the best ORR catalyst and is widely used in fuel cells. However, Pt is one of the most expensive metals on Earth. On the other hand, for OER catalysis, iridium (Ir), ruthenium (Ru), and their oxides [10,11] are commonly used, although they are very expensive materials. With this in mind, researchers are mainly focused on finding alternative catalysts for ORR and OER catalysis composed of cheap, earth-abundant materials. Some of the most promising alternatives are transition metals, their oxides, and compounds, which are heavily investigated for ORR, OER, and bifunctional applications [12–14].

Recently, a catalyst based on Fe and Co nanoparticles (NPs) incorporated in N-doped honeycombed carbon (FeCo@N-HC) was synthesized by Han and co-workers and tested as an ORR/OER bifunctional catalyst in alkaline media [15]. Their catalyst showed good performance for ORR and OER catalysis, with an ORR half-wave potential of 0.85 V and achieving  $10 \text{ mA cm}^{-2}$  in OER mode at an overpotential of 318 mV. The synergistic effect between FeCo NPs and honeycomb-like carbon led to their catalyst's good bifunctional performance, which showed reasonable stability in alkaline media. Kisand et al. have synthesized trimetallic NiFeCo on N-doped carbon (NiFeCoNC) that exhibited a half-wave potential of 0.84 V and achieved  $10 \text{ mA cm}^{-2}$  in OER mode at an overpotential of 360 mV [16]. The  $\Delta E$  value was found to be 0.75 V, indicating its good bifunctional performance, which authors attributed to their novel synthesis procedure that led to a hierarchically porous structure with evenly dispersed N-coordinated transition metal active sites. Sun and co-workers synthesized bifunctional perovskite oxide ( $\text{LaMnNiCoO}_3$  (1:2:3)) that reached OER  $10 \text{ mA cm}^{-2}$  at an overpotential of 370 mV with an ORR half-wave potential of 0.75 V and an  $\Delta E$  of 0.85 V in 0.1 M KOH [17]. They also showed that dual metal dopants can precisely tailor the catalysts' electronic structures, enabling activity for both ORR and OER. Bimetallic hollow tubular  $\text{NiCoO}_x$  was developed by Xue et al. and tested in 0.1 M KOH [18]. Their best-performing material,  $\text{Ni}_{0.33}\text{Co}_{0.67}\text{O}_x$ , reached a diffusion-limiting current density of  $5.8 \text{ mA cm}^{-2}$  with a half-wave potential of 0.81 V and overpotential of 281 mV to reach an OER current density of  $10 \text{ mA cm}^{-2}$ . The well-defined core-shell structure of hollow tubes with nanosheets rooted on its surface offers a large specific surface area, and the synergistic effect from Ni and Co on the bimetallic oxide leads to good bifunctional performance.

In the authors' previous study, Pt- and PtNi-decorated  $\text{Mn}_2\text{O}_3$ -NiO binary metal oxides (BMOs) were synthesized via microwave radiation and tested as ORR/OER bifunctional catalysts in 0.1 M KOH [19]. Pt/ $\text{Mn}_2\text{O}_3$ -NiO and PtNi/ $\text{Mn}_2\text{O}_3$ -NiO reached diffusion-limiting current densities of  $-4.5$  and  $-4.3 \text{ mA cm}^{-2}$ , respectively, and reached an OER current density of  $10 \text{ mA cm}^{-2}$  at an overpotential of 542 and 529 mV, respectively. Good bifunctional performance was confirmed by  $\Delta E$  values of 0.97 and 0.98 V for PtNi/ $\text{Mn}_2\text{O}_3$ -NiO and Pt/ $\text{Mn}_2\text{O}_3$ -NiO, respectively. The results obtained suggest that NiO was the active site for OER while ORR mainly occurred on PtNi NPs.

This study reports the synthesis of  $\text{Mn}_2\text{O}_3$ -NiO binary metal oxides and a series of N-doped  $\text{Mn}_2\text{O}_3$ -NiO decorated with either Pt, Ni, or PtNi nanoparticles; the characterization of their structures and compositions and the assessment of their ORR/OER bifunctional performance in 0.1 M KOH.

## 2. Experimental

### 2.1. Support Material Synthesis

The starting materials for binary oxide preparation,  $\text{Mn}(\text{NO}_3)_2 \cdot 4\text{H}_2\text{O}$  ( $\geq 98.5$  wt.%, Merck, Darmstadt, Germany), nickel (II) acetylacetonate ( $\text{Ni}(\text{C}_5\text{H}_7\text{O}_2)_2$ ,  $\geq 95$  wt.%, Sigma-Aldrich, St. Louis, MO, USA), ammonia solution ( $\text{NH}_3$ , 25 wt.% in water), and ethanol (absolute), were purchased from Fluka Company (Buchs, Switzerland) and used without further purification. Deionized water was used to prepare all solutions.

$\text{Mn}_2\text{O}_3$ -NiO powders were prepared by co-precipitation, which differed from the approach followed in the authors' previous study [19]. The typical steps were as follows: 0.015 mol of  $\text{Mn}(\text{NO}_3)_2 \cdot 4\text{H}_2\text{O}$  and 0.015 mol of  $[\text{Ni}(\text{C}_5\text{H}_7\text{O}_2)_2]$  were dissolved in 150 mL of 2 M  $\text{HNO}_3$  and 150 mL of 6 M  $\text{NaOH}$  solutions separately, and each stirred for 0.5 h at room temperature. Two mixtures were then mixed in a 1:1 molar ratio and stirred for about 1 h to obtain a stable mixture. This mixture was precipitated by gradually adding  $\text{NH}_3$  solution until the pH reached 11. The resultant solution was slowly stirred at 75 °C for 5 h. The resulting precipitate was filtrated and sequentially washed with ultrapure water and ethanol (absolute) to remove  $\text{NO}_3^-$  anions. Finally, the precipitate was dried at 80 °C for 12 h and calcinated at 450 °C for 4 h. The resultant  $\text{Mn}_2\text{O}_3$ -NiO powders were ground at a constant vibration rate of 300 rpm for 10 min in a Retsch MM 200 vibrant-ball mill (Retsch Co., Ltd., Hann, Germany).

### 2.2. Nitrogen Doping and Catalyst Synthesis

Melamine (Sigma Aldrich, St. Louis, MO, USA) was used as a nitrogen source for the synthesis of the N-doped  $\text{Mn}_2\text{O}_3$ -NiO structure.  $\text{Mn}_2\text{O}_3$ -NiO and melamine were physically mixed in a mortar in mass ratios of (1:1), (1:2), and (2:1) until a homogeneous appearance was apparent. The mixture was then transferred to crucibles, and the tube was placed in the furnace. To provide an inert environment in the furnace before the heat treatment, nitrogen gas was allowed to pass at a low flow rate, and gas flow was continued throughout the heat treatment. Then, the temperature of the furnace was set to 400 °C, and the samples were kept under nitrogen flow for 2 h after the furnace reached this temperature. At the end of this period, the heating was terminated, and the samples were allowed to cool under nitrogen flow without being exposed to air until the temperature of the furnace approached ambient temperature. The samples were then removed from the oven and stored in sealed containers [20]. These support materials doped with different amounts of melamine were named  $\text{Mn}_2\text{O}_3$ -NiO-N (1:1),  $\text{Mn}_2\text{O}_3$ -NiO-N (1:2), and  $\text{Mn}_2\text{O}_3$ -NiO-N (2:1), respectively.

The microwave-assisted polyol method was preferred for the simple and efficient preparation of nitrogen-doped  $\text{Mn}_2\text{O}_3$ -NiO-N supported Pt- and Ni-containing catalysts. This method can heat the solution quickly and homogeneously due to microwave heating, thus saving time and energy. The author's previous work [21] outlines the catalyst synthesis. Here, ethylene glycol (Sigma Aldrich, St. Louis, MO, USA) was used as the reducing agent, the precursor of  $\text{H}_2\text{PtCl}_6 \cdot 6\text{H}_2\text{O}$  (Sigma Aldrich, St. Louis, MO, USA), and  $\text{NiCl}_2 \cdot 6\text{H}_2\text{O}$  (Sigma Aldrich, St. Louis, MO, USA), and the nominal metal loading on the support material was targeted as 20 wt.%. This amount was adjusted to 10 wt.% Pt and 10 wt.% Ni in the bimetallic catalyst structure. Initially, 0.05 M solutions were prepared by dissolving Pt and Ni salt precursors separately in pure water. The solutions were added to a beaker containing 50 mL of ethylene glycol based on the calculated amount for synthesizing the catalyst, taking into account its metal content. This mixture was mixed with a magnetic stirrer for 15 min, and at the end of the period, the relevant support material was added to the mixture. The mixing continued for 60 min. Then, the solution was placed in a household microwave oven (Samsung, Suwon-si, Republic of Korea) and kept at 800 W heating power for 60 s. At the end of this period, the solution was rapidly cooled in an ice bath. Centrifugation was performed at 7000 rpm to separate the synthesized catalyst from the solution. At the end of the process, the remaining solid was washed with acetone and pure water, and centrifugation was performed after each washing process. The solid

material obtained at the end of the process was dried under vacuum in an oven set at 100 °C for 12 h. The same procedure was followed in the preparation of all catalysts. After the catalyst synthesis process,  $\text{Mn}_2\text{O}_3$ -NiO-N-supported catalysts containing Pt and Ni metals were obtained.

Experimental details of materials' physical characterization and electrochemical measurements are given in the Supplementary Material.

### 3. Results and Discussion

#### 3.1. Catalyst Characterization

The amount of nitrogen in the structure of the support materials was determined by elemental analysis (Figure S1). The results show that the nitrogen doping process was carried out successfully. As the amount of melamine mixed with the support material before the pyrolysis process increases, the amount of added nitrogen also increases.

Additionally, a color change was observed in the  $\text{Mn}_2\text{O}_3$ -NiO sample depending on the amount of added nitrogen source (Figure S2). As the amount of nitrogen doping increased, the color of the sample changed from almost black to shades of brown.

Figure 1a–d shows SEM images and EDS analysis results taken at different magnifications for  $\text{Mn}_2\text{O}_3$ -NiO and  $\text{Mn}_2\text{O}_3$ -NiO-N (1:1) support materials. These analyses elucidated the morphological structure of the support samples after nitrogen doping. The SEM images taken at 1  $\mu\text{m}$  and 200 nm magnifications show that small porous structures were formed in the surface morphology with the doping of nitrogen on the  $\text{Mn}_2\text{O}_3$ -NiO structure (Figure 1b). In addition, the elements contained in the support materials were confirmed by using the EDS analysis (Figure 1c,d). The N peak in the  $\text{Mn}_2\text{O}_3$ -NiO-N sample shows that the doping process was carried out successfully (Figure 1d).

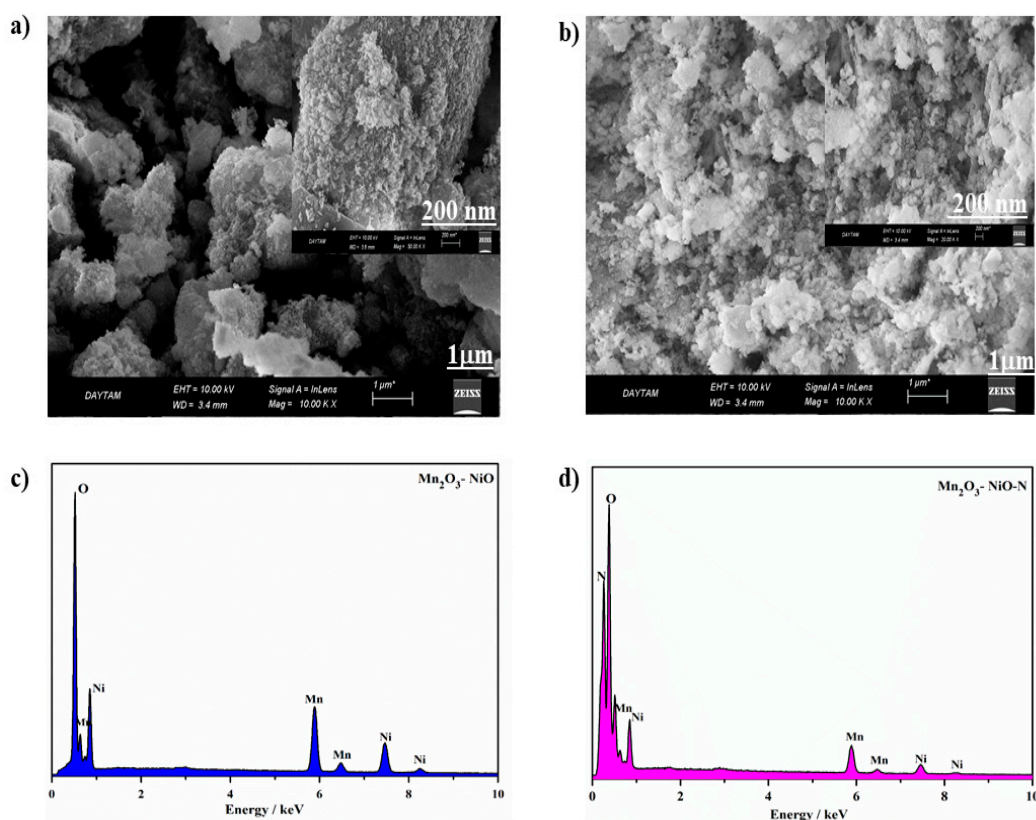


**Figure 1.** SEM images and EDS spectra of (a,c)  $\text{Mn}_2\text{O}_3$ -NiO and (b,d)  $\text{Mn}_2\text{O}_3$ -NiO-N (1:1).

The structural properties of the synthesized support materials, such as surface area, pore structure, and pore volume, are among the critical parameters affecting the catalyst's

performance. As such, the activity of the catalyst is related to the surface area of the reacting catalyst and the size of the catalyst particles. The results of the BET analysis performed to elucidate the structure of the synthesized support materials are given in Figure S3. The nitrogen adsorption–desorption isotherms of the synthesized catalysts comply with the Type-IV isotherm based on the hysteresis loop shapes determined by IUPAC. In the characteristic features of Type-IV hysteresis isotherms, meso- and micropores exist together in the structure [21]. Table 1 provides information on the structural properties of the  $\text{Mn}_2\text{O}_3$ -NiO samples based on BET analysis. It is seen that the surface area decreased significantly with the addition of melamine to the  $\text{Mn}_2\text{O}_3$ -NiO sample. This is explained by the decrease in the BET surface area and total pore volume and the increase in the average pore width due to the blockage or even collapse of some pores in the structure with nitrogen doping [22].

**Table 1.** BET analysis results of the  $\text{Mn}_2\text{O}_3$ -NiO materials.

Sample	BET Surface Area ( $\text{m}^2 \text{g}^{-1}$ )	BJH Adsorption Cumulative Pore Volume ( $\text{cm}^3 \text{g}^{-1}$ )	BJH Desorption Cumulative Pore Volume ( $\text{cm}^3 \text{g}^{-1}$ )	BJH Adsorption Average Pore Width (nm)	BJH Desorption Average Pore Width (nm)
$\text{Mn}_2\text{O}_3$ -NiO	73.11	0.465	0.465	23.0	16.5
$\text{Mn}_2\text{O}_3$ -NiO-N (1:1)	16.19	0.143	0.143	31.3	22.8
$\text{Mn}_2\text{O}_3$ -NiO-N (1:2)	3.16	0.058	0.063	31.2	21.3
$\text{Mn}_2\text{O}_3$ -NiO-N (2:1)	37.52	0.219	0.220	24.6	20.4

When the XPS spectrum of the nitrogen-doped support materials is looked at, in general, five different peaks can be seen (Figure 2a). These peaks are attributed to Ni, Mn, O, N, and C elements [19–24]. The presence of Ni, Mn, and O elements in the general spectrum of the synthesized catalysts was due to the support material. By adding melamine to the structure of the support material, the presence of the N peak showed that the nitrogen-doping process was successfully accomplished. In addition, the presence of the C peak was caused by the C atoms in the structure of the melamine used in the doping process. N1s partial XPS spectra taken in the 390–410 eV range of  $\text{Mn}_2\text{O}_3$ -NiO-N support that the materials doped with nitrogen in different amounts were deconvoluted (Figure 2b–d) [25]. The deconvoluted N 1s XPS spectra evidence two different chemical bonds between N atoms with atoms in the  $\text{Mn}_2\text{O}_3$ -NiO structure. The peaks at binding energies of  $398.1 \pm 0.1$  eV and  $403.0 \text{ eV} \pm 0.1$  represent pyridinic-N and N-oxide, respectively. The low-energy component of the N1s spectra, at a binding energy of about 398.1 eV, is attributed to the formation of chemical N-Mn or N-Ni bonds, resulting from the replacement of O atoms with N atoms in the N-doped  $\text{Mn}_2\text{O}_3$ -NiO structures. The other low-intensity peak corresponds to  $\pi$  excitations that cause a positive charge accumulation in the N species located at the edges [26,27]. Significant shifts occurred in the peaks depending on the change in the amount of N doped (Figure 2e). Among all structures, it is seen that the pyridinic-N peak is more prominent and closer to the binding energy value in the sample with a high N-doping rate.

The ICP-MS technique was used to determine the amount of Pt and Ni metal loadings on the support material in the synthesized catalysts (Table S1). The results show that all catalysts contain Pt or Ni at values close to the nominal 20 wt. % metal content.

The XRD spectra of the synthesized catalysts are given in Figure 3a–c. The (211), (222), (400), (431), (440), and (622) peaks representing the  $\text{Mn}_2\text{O}_3$  structure are found in the XRD spectra of all the catalysts. The diffraction angles of these peaks are indicated as  $23.1^\circ$ ,  $32.9^\circ$ ,  $38.2^\circ$ ,  $49.3^\circ$ ,  $55.1^\circ$ , and  $65.7^\circ$ , respectively [28]. Again, in all catalyst structures, the diffraction peaks assigned to reflections from the NiO planes (111), (200), (220), (311), and (222) occur at  $2\theta$  values of  $37.2^\circ$ ,  $43.2^\circ$ ,  $62.8^\circ$ ,  $75.2^\circ$ , and  $79.3^\circ$ , respectively [29]. In addition, the peaks of the  $\text{NiMn}_2\text{O}_4$  structure are present in all catalysts. This structure is attributed to the planes (111), (200), (311), and (511) defined at the values of  $18.5^\circ$ ,  $30.5^\circ$ ,  $35.9^\circ$ ,  $43.6^\circ$ , and  $57.2^\circ$  of  $2\theta$  [30]. The peaks of the Pt metal loaded on the  $\text{Mn}_2\text{O}_3$ -NiO-N support material correspond to the  $2\theta$  values of the face-centered cubic (fcc) crystal structure at

40.1°, 46.5°, 68.0°, and 81.9°, respectively, (111), (200), (220), and (311) [31] (Figure 3a,c). The Ni used in the catalyst structure has an fcc structure with peaks at 2θ, 45°, 52.3°, and 77.4° in the (111), (200), and (220) planes [32] (Figure 3b,c). It can be seen that the peaks of the metals in all catalyst structures are broader and flattened. The addition of metals to the Mn<sub>2</sub>O<sub>3</sub>-NiO structure resulted in the shifting of the Mn<sub>2</sub>O<sub>3</sub> and NiO peaks towards the lower 2θ angles (Figure 3d). This shows the change in the lattice structure with the addition of Pt and Ni to the Mn<sub>2</sub>O<sub>3</sub>-NiO structure. In addition, with the effect of the bimetallic structure formed in PtNi/Mn<sub>2</sub>O<sub>3</sub>-NiO-N catalysts in which both metals participate in the structure, there are shifts in the Pt and Ni peaks, along with the peaks representing that some planes of Ni are not clearly seen.

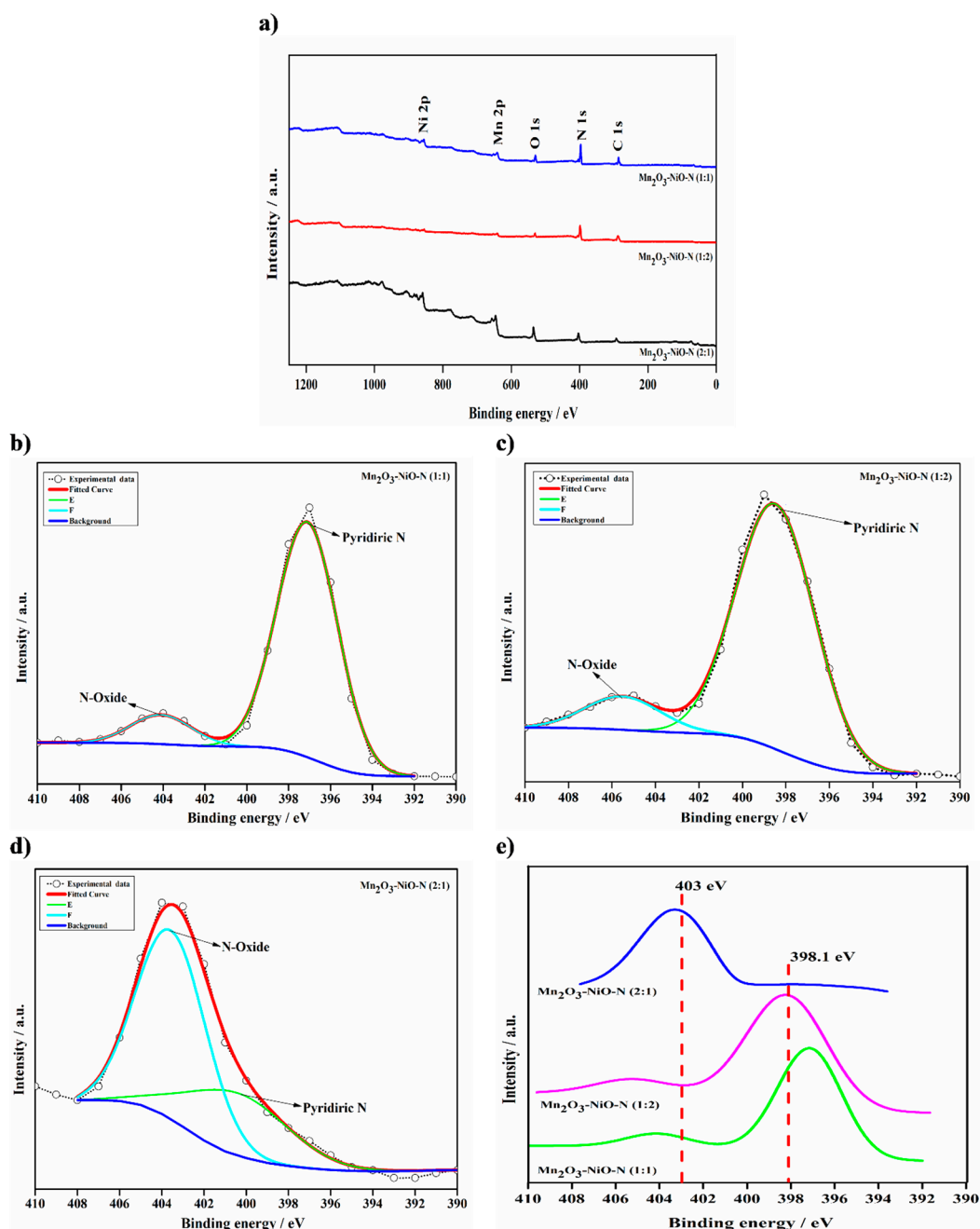


**Figure 2.** XPS spectra of N-doped Mn<sub>2</sub>O<sub>3</sub>-NiOs: (a) general spectra; (b–d) N 1s spectra with deconvoluted peaks; and (e) a comparison of the N 1s spectra.

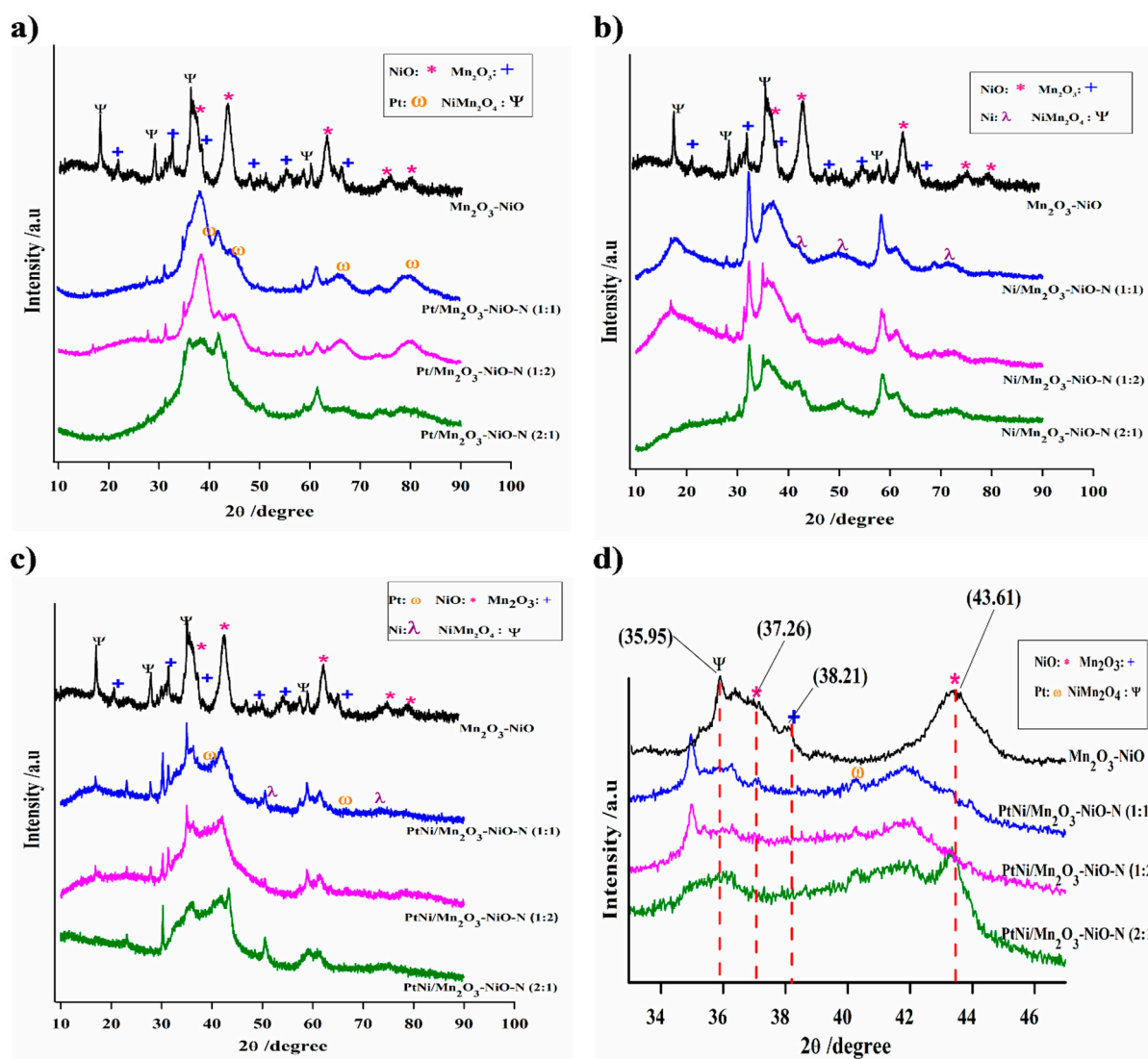


**Figure 3.** XRD patterns of (a) Pt/Mn<sub>2</sub>O<sub>3</sub>-NiO-N, (b) Ni/Mn<sub>2</sub>O<sub>3</sub>-NiO-N, and (c) PtNi/Mn<sub>2</sub>O<sub>3</sub>-NiO-N catalysts, and (d) magnified XRD peak shift of PtNi/Mn<sub>2</sub>O<sub>3</sub>-NiO-N catalysts.

### 3.2. Double-Layer Capacitance Investigation

To investigate the double-layer capacitance of each electrocatalyst, CVs at different scan rates were recorded in a  $\pm 100$  mV potential window near the open-circuit potential (OCP) followed by plotting  $\Delta j = f(\nu)$ , where  $\Delta j = (j_a - j_c)/2$  (mA cm<sup>-2</sup>) and  $\nu$  is the electrode polarization rate (mV s<sup>-1</sup>). Capacitance was then determined as a slope of  $\Delta j/2 = f(\nu)$  plot for each electrocatalyst. Firstly, we investigated the  $C_{dl}$  of pure, undoped Mn<sub>2</sub>O<sub>3</sub>-NiO electrocatalyst (Figure S4). However, due to a deviation from the linearity observed for the  $\Delta j = f(\nu)$  plot at higher scan rates, determining the double-layer capacitance of pure undoped Mn<sub>2</sub>O<sub>3</sub>-NiO could not be performed with high precision. Also, a slight distortion of CVs with an increase in scan rate was observed for all samples, indicating the existence of ohmic resistance in parallel with  $C_{dl}$  [33].

Figure S5 shows the CVs at different scan rates of nitrogen-doped Mn<sub>2</sub>O<sub>3</sub>-NiO with three different N-to-Mn<sub>2</sub>O<sub>3</sub>-NiO ratios. The oxides showed double-layer capacitances and corresponding ECSA values of the same order of magnitude, i.e.,  $C_{dl}$  of 2.29 mF cm<sup>-2</sup> and ECSA of 57.3 cm<sup>2</sup> for Mn<sub>2</sub>O<sub>3</sub>-NiO-N (1:1),  $C_{dl}$  of 2.14 mF cm<sup>-2</sup> and ECSA of 53.5 cm<sup>2</sup> for Mn<sub>2</sub>O<sub>3</sub>-NiO-N (2:1), and  $C_{dl}$  of 2.07 mF cm<sup>-2</sup> and ECSA of 51.8 cm<sup>2</sup> for Mn<sub>2</sub>O<sub>3</sub>-NiO-N (1:2).

The double-layer capacitance was also investigated for N-doped BMOs decorated with Pt (Figure S6) and Ni (Figure S7). It is evident that Pt-decorated materials showed significantly higher  $C_{dl}$  values than the N-doped BMOs decorated with Ni. The highest value was obtained for Pt/Mn<sub>2</sub>O<sub>3</sub>-NiO-N (2:1) ( $C_{dl}$  of 10.92 mF cm<sup>-2</sup> corresponding to ECSA of 273.0 cm<sup>2</sup>), while for Pt/Mn<sub>2</sub>O<sub>3</sub>-NiO-N (1:1) and Pt/Mn<sub>2</sub>O<sub>3</sub>-NiO-N (1:2)  $C_{dl}$  they were calculated as 9.72 and 5.70 mF cm<sup>-2</sup>, respectively, corresponding to ECSA values of 243.0 and 142.5 cm<sup>2</sup>.

Amongst Ni-decorated materials, the highest  $C_{dl}$  was calculated for Ni/Mn<sub>2</sub>O<sub>3</sub>-NiO-N (2:1), 1.67 mF cm<sup>-2</sup>, corresponding to an ECSA of 41.8 cm<sup>2</sup>. Ni/Mn<sub>2</sub>O<sub>3</sub>-NiO-N (1:1) and Ni/Mn<sub>2</sub>O<sub>3</sub>-NiO-N (1:2) had  $C_{dl}$  values of 1.40 and 1.44 mF cm<sup>-2</sup>, respectively. These values correspond to ECSA values of 36.0 and 35.0 cm<sup>2</sup>, respectively.

Finally, a double-layer capacitance investigation was performed for PtNi/Mn<sub>2</sub>O<sub>3</sub>-NiO-N with three different BMO-to-N ratios (Figure S8). As with the pure N-doped BMOs, no significant difference was observed between the three samples. PtNi/Mn<sub>2</sub>O<sub>3</sub>-NiO-N (2:1) showed a  $C_{dl}$  of 1.92 mF cm<sup>-2</sup> and a corresponding ECSA of 48.0 cm<sup>2</sup>, PtNi/Mn<sub>2</sub>O<sub>3</sub>-NiO-N (1:2) a  $C_{dl}$  of 1.81 mF cm<sup>-2</sup> and an ECSA of 45.3 cm<sup>2</sup>, and PtNi/Mn<sub>2</sub>O<sub>3</sub>-NiO-N (1:1) a  $C_{dl}$  of 1.76 mF cm<sup>-2</sup> and an ECSA of 44.0 cm<sup>2</sup>. A comparison of all the calculated  $C_{dl}$  values, as well as the ECSA and BET surface area values, are presented in Table S2.

### 3.3. Activity towards ORR

The ORR is one of the most critical reactions in modern electrochemistry. It is the core reaction for most electrochemical energy conversion and storage devices such as fuel cells and metal–air batteries. In alkaline media, it can generally proceed via the direct four-electron reduction of molecular O<sub>2</sub> to OH<sup>-</sup>, or via the two-electron mechanism, which involves a peroxide ion as an intermediary species. Four-electron reduction is generally desirable for electrochemical energy storage and conversion due to its faster kinetics and no loss of reactant species in the form of an intermediary [9,34–37]. However, the two-electron mechanism can also be useful in some systems, such as hydrogen peroxide production.

#### 3.3.1. ORR Activity of Pure and N-Doped Mn<sub>2</sub>O<sub>3</sub>-NiO

To investigate the ORR activity of Mn<sub>2</sub>O<sub>3</sub>-NiO BMO, CVs were first recorded at 0 rpm in the N<sub>2</sub> and O<sub>2</sub> atmosphere (Figure 4a), followed by a series of LSVs at different rotation rates in the O<sub>2</sub> atmosphere (Figure 4b).

From the acquired LSVs, the ORR peak position and the limiting current density at 1800 rpm were determined to compare the activity of the different electrocatalysts. For pure Mn<sub>2</sub>O<sub>3</sub>-NiO, the  $j_d$  was  $-1.93$  mA cm<sup>-2</sup> at 1800 rpm. LSV at 1800 rpm also enabled the determination of the half-wave potential,  $E_{1/2}$ , as another key parameter for assessing ORR activity. For pure Mn<sub>2</sub>O<sub>3</sub>-NiO, an  $E_{1/2}$  value of 0.66 V was found.

Doping of pure Mn<sub>2</sub>O<sub>3</sub>-NiO with nitrogen in different ratios increased the value of the limiting current density at 1800 rpm to  $-2.75$  mA cm<sup>-2</sup> for Mn<sub>2</sub>O<sub>3</sub>-NiO-N (1:1),  $-2.62$  mA cm<sup>-2</sup> for Mn<sub>2</sub>O<sub>3</sub>-NiO-N (2:1), and  $-2.29$  mA cm<sup>-2</sup> for Mn<sub>2</sub>O<sub>3</sub>-NiO-N (1:2), as seen in Figure 5d–f. N-doping also had a positive effect on increasing the value of  $E_{1/2}$ . The half-wave potential was increased to 0.67 V, 0.70 V, and 0.75 V for Mn<sub>2</sub>O<sub>3</sub>-NiO-N (1:2), Mn<sub>2</sub>O<sub>3</sub>-NiO-N (2:1), and Mn<sub>2</sub>O<sub>3</sub>-NiO-N (1:1), respectively, indicating faster kinetics of ORR on N-doped BMOs. These faster ORR kinetics might come from the somewhat larger pore size, facilitating the diffusion of reactants and intermediates to/from the active sites, Table 1. The presence of pyridinic-N facilitates the transfer of electrons towards active sites and thus further boosts the ORR kinetics.

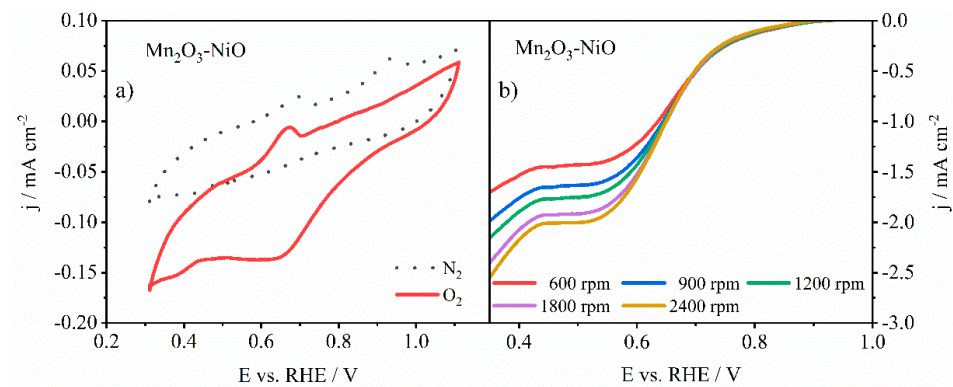


**Figure 4.** (a) CVs with  $\text{Mn}_2\text{O}_3\text{-NiO}$  in  $\text{N}_2$ - and  $\text{O}_2$ -saturated 0.1 M KOH and (b) LSVs at  $10 \text{ mVs}^{-1}$  and different rotation rates of the same material.

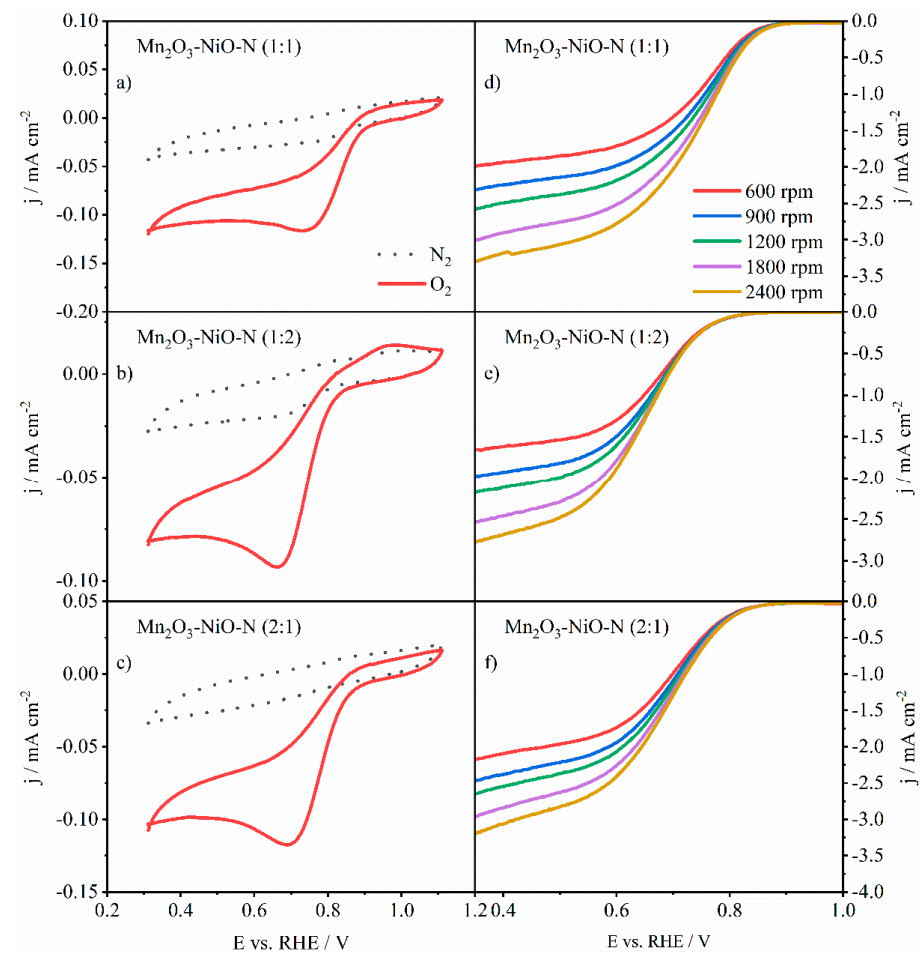


**Figure 5.** (a–c) CV experiments with N-doped  $\text{Mn}_2\text{O}_3\text{-NiO}$  with three different N-to-BMO ratios in  $\text{N}_2$ - and  $\text{O}_2$ -saturated 0.1 M KOH and (d–f) LSVs at different rotation rates of the same materials.

LSVs at 1800 rpm were subjected to Tafel analysis, as can be seen in Figure S9a. The highest Tafel slope was calculated for pure  $\text{Mn}_2\text{O}_3\text{-NiO}$  ( $151 \text{ mV dec}^{-1}$ ), while all three N-doped samples showed a lower value of this parameter, further corroborating faster ORR kinetics at N-doped BMOs. For  $\text{Mn}_2\text{O}_3\text{-NiO-N (1:1)}$ ,  $\text{Mn}_2\text{O}_3\text{-NiO-N (1:2)}$ , and  $\text{Mn}_2\text{O}_3\text{-NiO-N (2:1)}$ , the Tafel slope values were calculated as 82, 90, and 99  $\text{mV dec}^{-1}$ , respectively.

Figure S9b presents the Koutecký–Levich (K-L) analysis for all the samples using data from LSV experiments at different rotation rates. By performing K-L analysis, the number of exchanged electrons,  $n$ , in the elementary step of the reaction was calculated for each tested electrocatalyst. For pure  $\text{Mn}_2\text{O}_3\text{-NiO}$ , the  $n$  value was 2.90 electrons, while for the N-doped samples, calculated values were 2.73, 2.35, and 3.63  $e^-$  for  $\text{Mn}_2\text{O}_3\text{-NiO-N}$  (1:1),  $\text{Mn}_2\text{O}_3\text{-NiO-N}$  (1:2), and  $\text{Mn}_2\text{O}_3\text{-NiO-N}$  (2:1), respectively. It should be mentioned that although K-L analysis is the standard method of determining the number of exchange electrons, it was derived for a single one-electron transfer with a preceding reaction of the first order [38–41].

### 3.3.2. ORR Activity of Pt-Decorated N-Doped $\text{Mn}_2\text{O}_3\text{-NiO}$

After establishing a baseline by testing pure and N-doped  $\text{Mn}_2\text{O}_3\text{-NiO}$ , Pt-decorated N-doped BMOs activity was assessed by performing LSV and CV investigations in the ORR potential range, Figure 6.

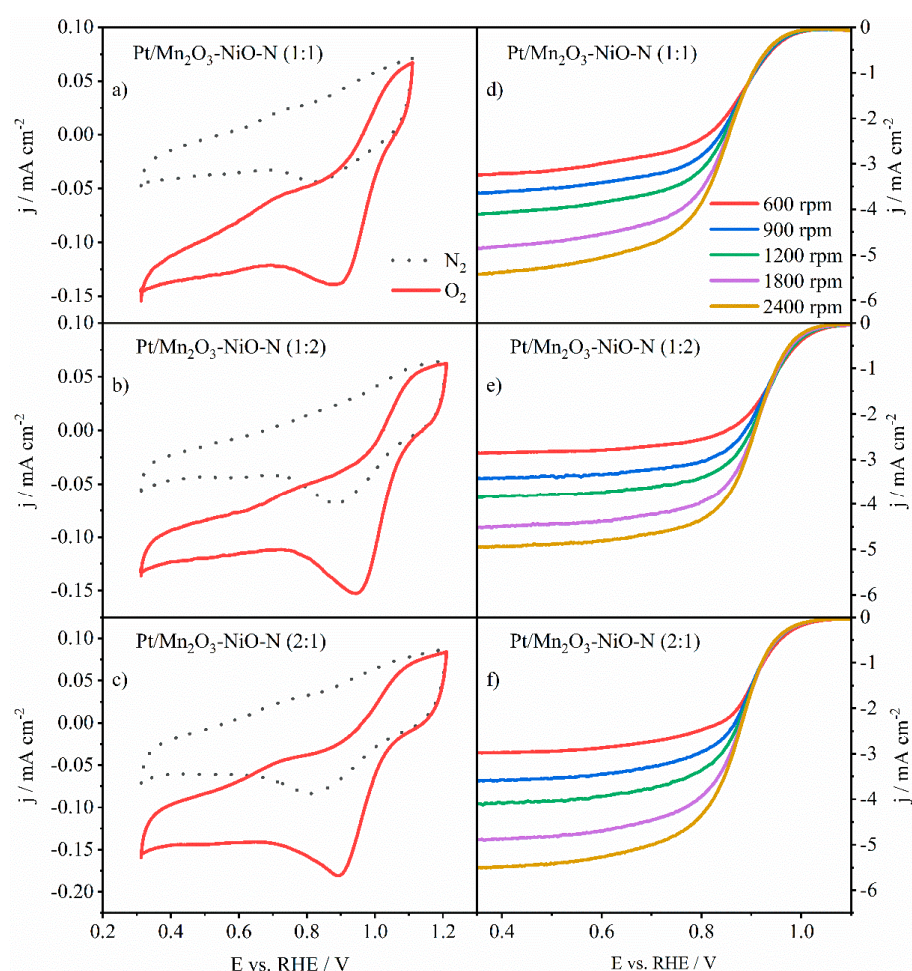


**Figure 6.** (a–c) CV experiments with Pt-decorated N-doped  $\text{Mn}_2\text{O}_3\text{-NiO}$  with three different N-to-BMO ratios in  $\text{N}_2$ - and  $\text{O}_2$ -saturated 0.1 M KOH and (d–f) LSVs at different rotation rates of the same materials.

As expected, decorating BMOs with platinum had positive effects on ORR performance. Pt-decorated materials showed higher diffusion-limiting current densities, lower-onset overpotential, and higher values of half-wave potential when compared to N-doped BMOs. The highest  $j_d$  was achieved with  $\text{Pt/Mn}_2\text{O}_3\text{-NiO-N}$  (2:1) ( $-4.81 \text{ mA cm}^{-2}$ ), which also had the highest value of kinetic current density ( $-6.71 \text{ mA cm}^{-2}$ ).  $\text{Pt/Mn}_2\text{O}_3\text{-NiO-N}$  (1:1) delivered a  $j_d$  and  $j_k$  of  $-4.69 \text{ mA cm}^{-2}$  and  $-2.97 \text{ mA cm}^{-2}$ , respectively, while

Pt/Mn<sub>2</sub>O<sub>3</sub>-NiO-N (1:2) delivered a  $j_d$  and  $j_k$  of  $-4.43 \text{ mA cm}^{-2}$  of  $-3.68 \text{ mA cm}^{-2}$ , respectively. The half-wave potential values were determined to be 0.92 V, 0.89 V, and 0.87 V for Pt/Mn<sub>2</sub>O<sub>3</sub>-NiO-N (1:2), Pt/Mn<sub>2</sub>O<sub>3</sub>-NiO-N (2:1), and Pt/Mn<sub>2</sub>O<sub>3</sub>-NiO-N (1:1), respectively.

The Tafel analysis (Figure S10a) showed similar results for Pt-decorated and non-decorated N-doped Mn<sub>2</sub>O<sub>3</sub>-NiO BMOs, with the lowest value of Tafel slope calculated for Pt/Mn<sub>2</sub>O<sub>3</sub>-NiO-N (1:1) of  $90 \text{ mV dec}^{-1}$ . As in the case of non-decorated BMOs, Pt/Mn<sub>2</sub>O<sub>3</sub>-NiO-N (1:1) was followed by Pt/Mn<sub>2</sub>O<sub>3</sub>-NiO-N (1:2) and Pt/Mn<sub>2</sub>O<sub>3</sub>-NiO-N (2:1), which had Tafel slopes of 92 and  $96 \text{ mV dec}^{-1}$ , respectively.

The Koutecký–Levich’s analysis of Pt/Mn<sub>2</sub>O<sub>3</sub>-NiO-N materials (Figure S10b) indicated that ORR on Pt-decorated materials mainly proceeds via the four-electron mechanism. For Pt/Mn<sub>2</sub>O<sub>3</sub>-NiO-N (1:1), Pt/Mn<sub>2</sub>O<sub>3</sub>-NiO-N (1:2), and Pt/Mn<sub>2</sub>O<sub>3</sub>-NiO-N (2:1), the number of exchanged electrons in the elementary step of reaction was calculated to be 3.88, 3.84, and 3.72, respectively. These values are somewhat higher than that for non-decorated material; however, these are expected because ORR on Pt generally occurs via the four-electron mechanism in alkaline solutions.

### 3.3.3. ORR Activity of Ni-Decorated N-Doped Mn<sub>2</sub>O<sub>3</sub>-NiO

To gain deeper insight into the role of Ni in decorating BMOs, we decorated the same set of non-decorated N-doped BMOs with Ni. As in the case of Pt-decorated materials, three materials were synthesized: Ni/Mn<sub>2</sub>O<sub>3</sub>-NiO-N (1:1), Ni/Mn<sub>2</sub>O<sub>3</sub>-NiO-N (1:2), and Ni/Mn<sub>2</sub>O<sub>3</sub>-NiO-N (2:1). As before, CV and LSV analysis was performed to gain insight into the electrochemical activity of these materials toward ORR, and the results are shown in Figure 7.

Unlike decorating with Pt, Ni-decorated materials showed the lowest values of  $j_d$  and  $j_k$  of all the tested materials. Ni/Mn<sub>2</sub>O<sub>3</sub>-NiO-N (1:1), Ni/Mn<sub>2</sub>O<sub>3</sub>-NiO-N (1:2), and Ni/Mn<sub>2</sub>O<sub>3</sub>-NiO-N (2:1) reached diffusion-limiting current densities at  $-0.83$ ,  $-1.21$ , and  $-1.18 \text{ mA cm}^{-2}$ , respectively, with kinetic current densities of  $-0.22$ ,  $-0.32$ , and  $-0.29 \text{ mA cm}^{-2}$ , respectively. Ni-decorated materials also showed a slight shift in half-wave potential toward negative potentials, indicating slower ORR kinetics on these materials. The  $E_{1/2}$  values for Ni/Mn<sub>2</sub>O<sub>3</sub>-NiO-N (1:1), Ni/Mn<sub>2</sub>O<sub>3</sub>-NiO-N (1:2), and Ni/Mn<sub>2</sub>O<sub>3</sub>-NiO-N (2:1) were calculated to be 0.60, 0.60, and 0.65 V, which is lower than both Pt-decorated and non-decorated BMOs.

Figure S11a shows the Tafel analysis for Ni-decorated BMOs. For Ni/Mn<sub>2</sub>O<sub>3</sub>-NiO-N (1:1), Ni/Mn<sub>2</sub>O<sub>3</sub>-NiO-N (1:2), and Ni/Mn<sub>2</sub>O<sub>3</sub>-NiO-N (2:1), the Tafel slope values were 86, 100, and  $87 \text{ mV dec}^{-1}$ , which are similar to or even slightly lower than that of Pt and non-decorated materials. Figure S11b presents the Koutecký–Levich analysis for the same Ni-decorated materials. The calculated  $n$  values for Ni/Mn<sub>2</sub>O<sub>3</sub>-NiO-N (1:1), Ni/Mn<sub>2</sub>O<sub>3</sub>-NiO-N (1:2), and Ni/Mn<sub>2</sub>O<sub>3</sub>-NiO-N (2:1) are 2.24, 3.17, and 3.97 electrons, respectively, indicating mixed kinetics for the first two materials. In comparison, the value of 3.97 electrons for Ni/Mn<sub>2</sub>O<sub>3</sub>-NiO-N (2:1) indicates a pure four-electron ORR mechanism. These results further suggest that the percentage of N-doping in Ni-decorated BMOs notably impacts ORR kinetics in these materials.

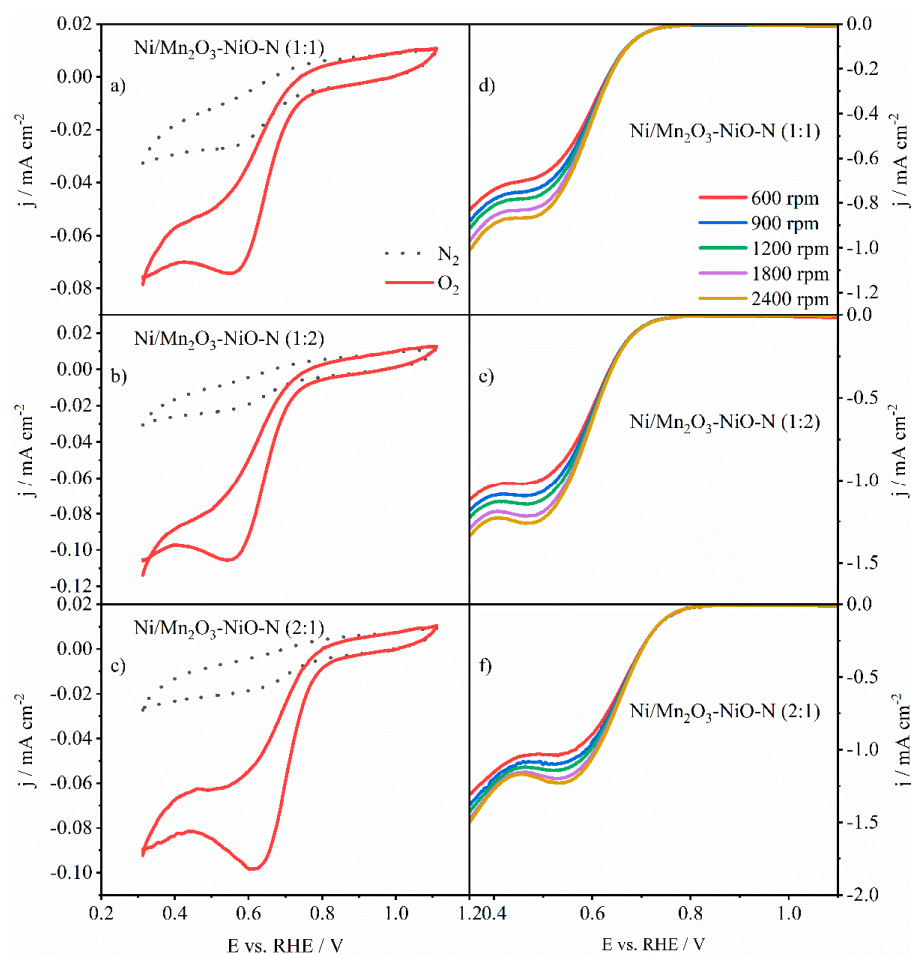


**Figure 7.** (a–c) CV experiments with Ni-decorated N-doped Mn<sub>2</sub>O<sub>3</sub>-NiO with three different N-to-BMO ratios in N<sub>2</sub> and O<sub>2</sub> saturated 0.1 M KOH and (d–f) LSVs at different rotation rates of the same materials.

### 3.3.4. ORR Activity of PtNi-Decorated N-Doped Mn<sub>2</sub>O<sub>3</sub>-NiO

After testing non-decorated, Pt-decorated, and Ni-decorated BMOs, N-doped BMOs decorated with both Pt and Ni were synthesized and tested. Having in mind the good results obtained with Pt-decorated materials and the good catalytic performance of Ni in terms of OER catalysis, decorating BMO with both Pt and Ni has promising potential in terms of synthesizing suitable bifunctional catalysts that will work in both ORR and OER mode. Furthermore, by introducing Ni to the material, one can lower the percentage of Pt, which effectively reduces the cost of the electrocatalyst.

To test the electrocatalytic performance toward ORR of PtNi-decorated N-doped BMOs, a series of CV and LSV experiments were performed in both N<sub>2</sub>- and O<sub>2</sub>-saturated 0.1 M KOH. The results of CV experiments are presented in Figure 8a–c, while the LSV results are shown in Figure 8d–f.

From the LSV results at different rotation rates, notably, the highest diffusion-limiting current density at 1800 rpm was achieved with PtNi/Mn<sub>2</sub>O<sub>3</sub>-NiO-N (1:2) ( $-2.94 \text{ mA cm}^{-2}$ ), followed by PtNi/Mn<sub>2</sub>O<sub>3</sub>-NiO-N (2:1) and PtNi/Mn<sub>2</sub>O<sub>3</sub>-NiO-N (1:1), with  $j_d$  values of  $-2.93$  and  $-1.64 \text{ mA cm}^{-2}$ , respectively. These values are somewhat smaller than that of purely Pt-decorated BMOs, which is expected with the lower percentage of Pt in bimetallic decorated BMOs. However, both the  $j_d$  and  $j_k$  were higher on the PtNi-decorated materials than those calculated for non-decorated and Ni-decorated BMOs (with the exception of PtNi/Mn<sub>2</sub>O<sub>3</sub>-NiO-N (1:1)). Furthermore, although smaller than that of Pt-decorated materials, the half-wave potentials calculated for PtNi/BMO-N has higher values than for BMO-N and Ni/BMO-N.  $E_{1/2}$  values were calculated as 0.70 and 0.65 V for PtNi/Mn<sub>2</sub>O<sub>3</sub>-

NiO-N (2:1) and PtNi/Mn<sub>2</sub>O<sub>3</sub>-NiO-N (1:1), respectively. The highest value of this parameter was calculated for PtNi/Mn<sub>2</sub>O<sub>3</sub>-NiO-N (1:2), 0.77 V, indicating the fastest ORR on this material among the three synthesized PtNi/BMO-N.

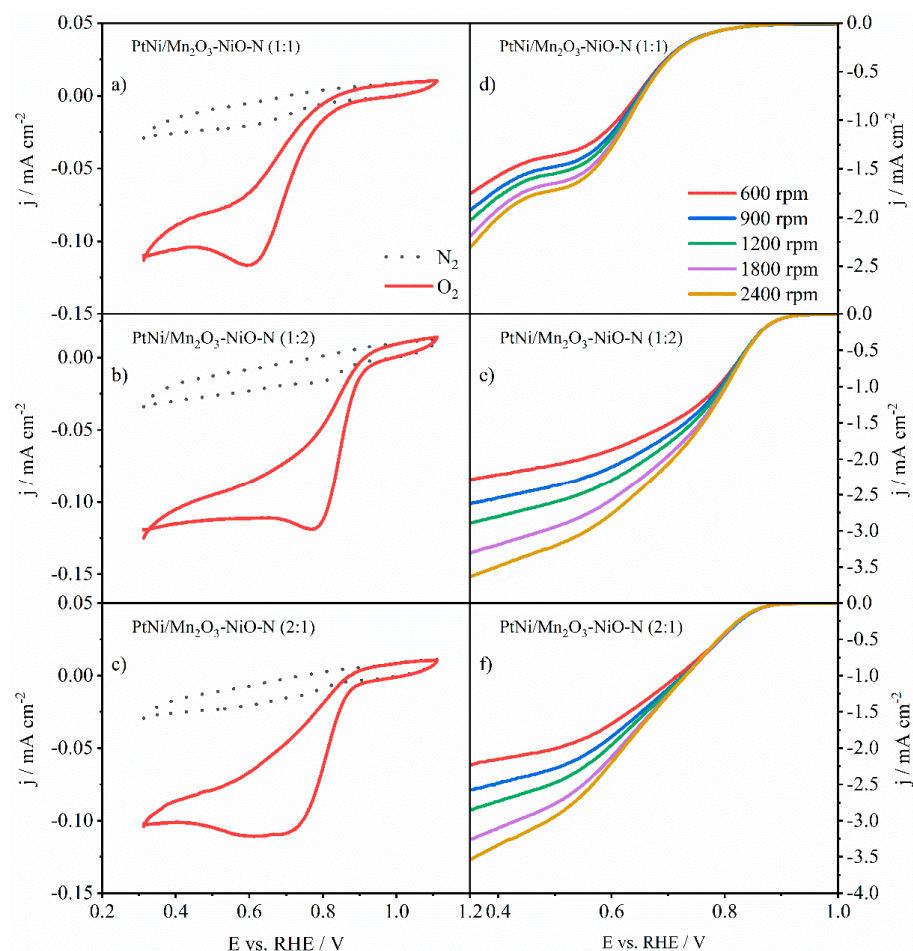


**Figure 8.** (a–c) CV experiments with PtNi-decorated N-doped Mn<sub>2</sub>O<sub>3</sub>-NiO with three different N-to-BMO ratios in N<sub>2</sub>- and O<sub>2</sub>-saturated 0.1 M KOH and (d–f) LSVs at different rotation rates of the same materials.

As for previous samples, the Tafel analysis for the three materials was performed with LSV data at 1800 rpm (Figure S12a). Of all tested materials in this work, PtNi/Mn<sub>2</sub>O<sub>3</sub>-NiO-N (2:1) and PtNi/Mn<sub>2</sub>O<sub>3</sub>-NiO-N (1:2) showed the lowest values of Tafel slope (both 67 mV dec<sup>-1</sup>), while PtNi/Mn<sub>2</sub>O<sub>3</sub>-NiO-N (1:1) showed a somewhat higher value of 129 mV dec<sup>-1</sup>. Given that the Tafel slope is closely related to the catalytic performance of the material, in terms that it represents the sensitivity of the electric current response to the applied potential [42], the lower b values for PtNi/Mn<sub>2</sub>O<sub>3</sub>-NiO-N (2:1) and PtNi/Mn<sub>2</sub>O<sub>3</sub>-NiO-N (1:2) indicates their superior activity toward ORR.

Figure S12b shows the Koutecký–Levich analysis for PtNi/BMO-N samples. As before, K-L plots are straight lines indicating the first-order reaction with respect to O<sub>2</sub> concentration [43]. For the three PtNi-decorated materials, the number of exchanged electrons was calculated to be between 3.38 and 3.82. The highest value of n was calculated for PtNi/Mn<sub>2</sub>O<sub>3</sub>-NiO-N (1:1) (n = 3.82), while the smallest value was calculated for PtNi/Mn<sub>2</sub>O<sub>3</sub>-NiO-N (1:2) (n = 3.38). For PtNi/Mn<sub>2</sub>O<sub>3</sub>-NiO-N (2:1), n was found to be 3.52, indicating that the ORR on these materials proceeds through the four-electron mechanism.

Even though PtNi-decorated materials showed somewhat lower values of diffusion-limiting current density and half-wave potentials than the BMOs decorated only with Pt, it should be noted that PtNi materials have only half of Pt loading in comparison with purely

Pt-decorated materials and one-quarter of commercial Pt/C (40 wt.%), making them a lot cheaper to produce. When the current densities are compared per mg of Pt, PtNi/BMO-N showed a higher current density per mg of Pt than Pt-decorated materials or even the commercial Pt/C, which was tested in a previous work [19].

### 3.4. OER Performance

As mentioned before, for an electrocatalyst to be considered bifunctional, it must be able to catalyze at least two desirable reactions in one system. For the oxygen side in URFCs, these two reactions are the reduction and evolution of oxygen. Therefore, LSV experiments were also performed in the OER potential range, see Figure 9. A peak at ca. 1.5 V can be attributed to the  $\text{Ni}^{2+}/\text{Ni}^{3+}$  redox peak, where the presence of Ni in a higher oxidation state normally favors the OER intermediates adsorption/desorption [44,45]. Thus,  $\text{Ni}^{2+}$ , along with  $\text{Ni}^{3+}$  species, is believed to be crucial for forming active sites for the catalysis of OER by Ni-based materials [46]. As with ORR, OER in alkaline media is a multistep process that includes a series of intermediate species.

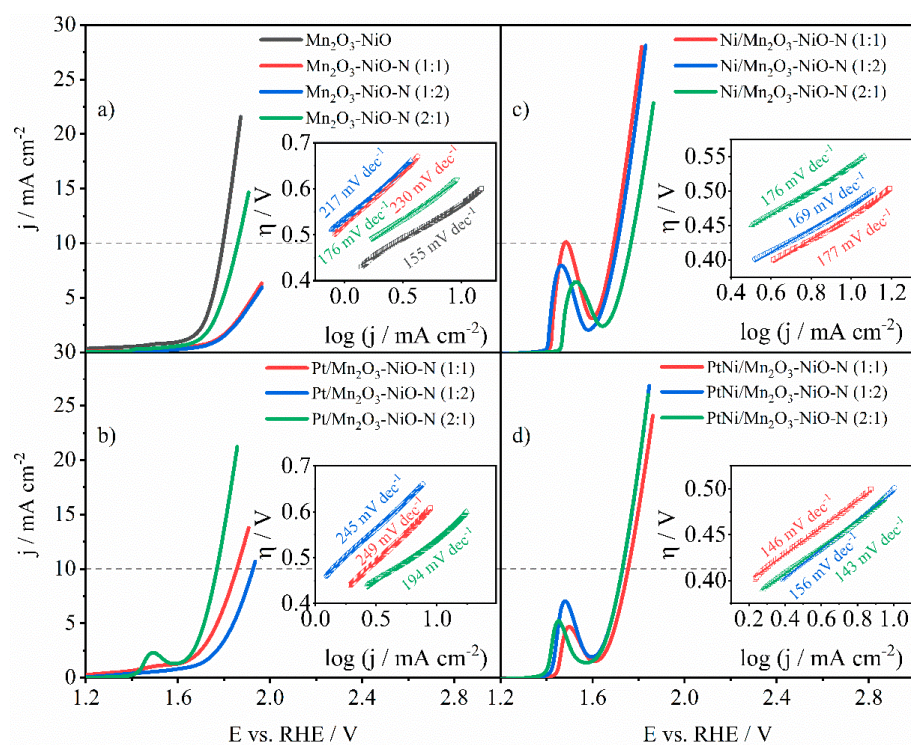


**Figure 9.** OER LSVs (iR-corrected) at 1200 rpm of (a) pure and N-doped  $\text{Mn}_2\text{O}_3\text{-NiO}$ , (b) Pt-decorated N-doped  $\text{Mn}_2\text{O}_3\text{-NiO}$ , (c) Ni-decorated N-doped  $\text{Mn}_2\text{O}_3\text{-NiO}$ , and (d) PtNi-decorated N-doped  $\text{Mn}_2\text{O}_3\text{-NiO}$ . Tafel analysis for these materials is presented as an inset in each graph.

Figure 9a presents the OER investigation of pure and N-doped BMOs with the Tafel plots in the inset. The lowest overpotential to achieve a benchmark current density of  $10 \text{ mA cm}^{-2}$  was acquired with pure  $\text{Mn}_2\text{O}_3\text{-NiO}$  (0.57 V), which also presented the lowest value in the Tafel slope ( $155 \text{ mV dec}^{-1}$ ). Of the three N-doped BMOs, a current density of  $10 \text{ mA cm}^{-2}$  was only achieved with  $\text{Mn}_2\text{O}_3\text{-NiO-N}$  (2:1) in the investigated potential range. The other two materials reached approximately  $6 \text{ mA cm}^{-2}$  at a potential of 2 V.  $\text{Mn}_2\text{O}_3\text{-NiO-N}$  (2:1) presented the lowest Tafel slope of  $176 \text{ mV dec}^{-1}$  compared to  $\text{Mn}_2\text{O}_3\text{-NiO-N}$  (1:1) ( $230 \text{ mV dec}^{-1}$ ) and  $\text{Mn}_2\text{O}_3\text{-NiO-N}$  (1:2) ( $217 \text{ mV dec}^{-1}$ ). The highest performance of undoped bimetallic oxide might be attributed to its notably higher BET surface area and pore volume, see Table 1. Namely, OER is not strictly limited to the surface, but is believed to proceed within a thin layer (for instance, 10 nm thicknesses) of the metal oxide. High porosity further facilitates accessibility of the active sites [44,47].

The results of OER investigation of Pt-decorated BMOs are presented in Figure 9b. As in the case of N-doped BMOs, the material with a BMO-to-N ratio of 2:1, Pt/Mn<sub>2</sub>O<sub>3</sub>-NiO-N (2:1), showed the lowest  $\eta_{10}$  value of 0.54 V, while for Pt/Mn<sub>2</sub>O<sub>3</sub>-NiO-N (1:1) and Pt/Mn<sub>2</sub>O<sub>3</sub>-NiO-N (1:2), these values were found to be 0.63 and 0.70 V, respectively. A similar trend was observed for Tafel slope values. As values of 194, 249, and 245 mV dec<sup>-1</sup> were calculated for Pt/Mn<sub>2</sub>O<sub>3</sub>-NiO-N (2:1), Pt/Mn<sub>2</sub>O<sub>3</sub>-NiO-N (1:1), and Pt/Mn<sub>2</sub>O<sub>3</sub>-NiO-N (1:2), respectively. The highest activity can be correlated with the highest ECSA and, thus, the highest number of active sites in the case of Pt/Mn<sub>2</sub>O<sub>3</sub>-NiO-N (2:1), see Table S2. Moreover, the mentioned conversion to the metal of a higher oxidation state evidenced by a peak at ca 1.5 V that favors OER was observed only in the case of Pt/Mn<sub>2</sub>O<sub>3</sub>-NiO-N (2:1), Figure 9b.

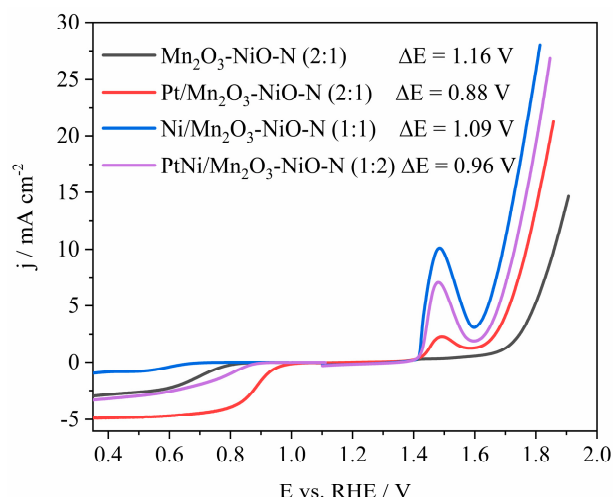
In the case of N-doped BMOs decorated with Ni (Figure 9c), deviation from the previously observed trend was noted. Namely, two materials with BMO-to-N ratios of 1:1 and 1:2 showed similar overpotential and current densities in the investigated potential range, while the third catalyst showed slightly worse results. Ni/Mn<sub>2</sub>O<sub>3</sub>-NiO-N (1:1) and Ni/Mn<sub>2</sub>O<sub>3</sub>-NiO-N (1:2) reached 10 mA cm<sup>-2</sup> at an overpotential of 0.46 and 0.48 V, respectively, while Ni/Mn<sub>2</sub>O<sub>3</sub>-NiO-N (2:1) reached this current value at an overpotential of 0.54 V. The Tafel slope values for all three catalysts were calculated as very similar, with Ni/Mn<sub>2</sub>O<sub>3</sub>-NiO-N (1:1), Ni/Mn<sub>2</sub>O<sub>3</sub>-NiO-N (1:2), and Ni/Mn<sub>2</sub>O<sub>3</sub>-NiO-N (2:1) showing b values of 177, 169, and 176 mV dec<sup>-1</sup>, respectively.

Figure 9d presents OER LSVs of PtNi-decorated N-doped BMOs, of which PtNi/Mn<sub>2</sub>O<sub>3</sub>-NiO-N (1:2) and PtNi/Mn<sub>2</sub>O<sub>3</sub>-NiO-N (2:1) reached 10 mA cm<sup>-2</sup> at an identical overpotential of 0.50 V, while PtNi/Mn<sub>2</sub>O<sub>3</sub>-NiO-N (1:1) reached this current value at an overpotential 30 mV higher. As is the case of Ni-decorated BMOs, the Tafel slope values were fairly similar for all three materials, with PtNi/Mn<sub>2</sub>O<sub>3</sub>-NiO-N (1:1), PtNi/Mn<sub>2</sub>O<sub>3</sub>-NiO-N (1:2), and PtNi/Mn<sub>2</sub>O<sub>3</sub>-NiO-N (2:1) showing b values of 146, 156, and 143 mV dec<sup>-1</sup>, respectively. It is worth mentioning that these Tafel slope values were the lowest of all the catalysts tested herein, while only Ni/Mn<sub>2</sub>O<sub>3</sub>-NiO-N (1:1) and Ni/Mn<sub>2</sub>O<sub>3</sub>-NiO-N (1:2) reached 10 mA cm<sup>-2</sup> at a slightly lower overpotential than PtNi-decorated N-doped BMOs.

### 3.5. Bifunctional Performance Assessment

As can be seen from the previously presented results, all four sample groups (BMO-N, Pt/BMO-N, Ni/BMO-N, and PtNi/BMO-N) showed fairly similar results among samples in the group, indicating that the percentage of N-doping has only a small effect on improving the catalytic performance. The impact of N-doping on catalytic performance can be seen when changing the ORR mechanism on some materials, switching from a two-electron mechanism to a four-electron mechanism, or vice versa.

To properly assess the bifunctional performance of the catalysts tested herein,  $\Delta E$  was calculated as the difference between the potential at which 10 mA cm<sup>-2</sup> was achieved in OER mode and half-wave potential in ORR mode,  $E_{10} - E_{1/2}$ , Figure 10 and Table 2. The smallest  $\Delta E$  values were calculated for Pt/Mn<sub>2</sub>O<sub>3</sub>-NiO-N (2:1) (0.88 V), Pt/Mn<sub>2</sub>O<sub>3</sub>-NiO-N (1:2) (0.94 V), and PtNi/Mn<sub>2</sub>O<sub>3</sub>-NiO-N (1:2) (0.96 V), followed by Pt/Mn<sub>2</sub>O<sub>3</sub>-NiO-N (1:1) ( $\Delta E = 0.99$  V). Other catalysts showed  $\Delta E$  values over 1 V (1.03–1.16 V), indicating somewhat worse bifunctional performance. It should be mentioned that bimetallic PtNi-decorated Mn<sub>2</sub>O<sub>3</sub>-NiO-N (1:2) had only half of the Pt loading in comparison with Pt-decorated materials, which makes this material significantly cheaper to produce with almost no loss in bifunctional performance. Furthermore, PtNi/Mn<sub>2</sub>O<sub>3</sub>-NiO-N (1:2) with an  $\Delta E$  of 0.96 V showed a slightly better  $\Delta E$  than the previously tested PtNi/Mn<sub>2</sub>O<sub>3</sub>-NiO ( $\Delta E = 0.97$  V) [19], indicating a slight improvement in bifunctional performance with the N-doping of Mn<sub>2</sub>O<sub>3</sub>-NiO BMO.



**Figure 10.** Bifunctional ORR/OER performance of the best electrocatalysts from each set of tested materials.

Figure 10 further indicates that different active sites are responsible for the two studied reactions, ORR and OER. Ni atoms in a higher oxidation state most likely act as highly active sites for OER [45,48]. Conversely, Pt in lower oxidation states most likely acts as catalytic sites for ORR [49]. Nitrogen present additionally facilitates electron transfer to these active sites [50].

**Table 2.** Comparison of ORR and OER parameters of the synthesized electrocatalysts with the literature data.

Material	$j_d/\text{mA cm}^{-2}$	ORR Parameters			$n$	OER Parameters		$\Delta E^*/V$	Electrolyte	Source
		$j_k/\text{mA cm}^{-2}$	$E_{1/2}/V$	$b/\text{mV dec}^{-1}$		$\eta_{10}/V$	$b/\text{mV dec}^{-1}$			
$\text{Mn}_2\text{O}_3\text{-NiO}$	-1.93	-0.67	0.66	151	2.90	0.57	155	1.14	0.1 M KOH	This work
$\text{Mn}_2\text{O}_3\text{-NiO-N (1:1)}$	-2.75	-1.65	0.75	82	2.73	-	230	-	0.1 M KOH	This work
$\text{Mn}_2\text{O}_3\text{-NiO-N (1:2)}$	-2.29	-1.26	0.67	90	2.35	-	217	-	0.1 M KOH	This work
$\text{Mn}_2\text{O}_3\text{-NiO-N (2:1)}$	-2.62	-1.00	0.70	99	3.63	0.63	176	1.16	0.1 M KOH	This work
$\text{Pt/Mn}_2\text{O}_3\text{-NiO-N (1:1)}$	-4.69	-2.97	0.87	90	3.88	0.63	249	0.99	0.1 M KOH	This work
$\text{Pt/Mn}_2\text{O}_3\text{-NiO-N (1:2)}$	-4.43	-3.68	0.92	92	3.84	0.70	245	0.94	0.1 M KOH	This work
$\text{Pt/Mn}_2\text{O}_3\text{-NiO-N (2:1)}$	-4.81	-6.71	0.89	96	3.72	0.54	194	0.88	0.1 M KOH	This work
$\text{Ni/Mn}_2\text{O}_3\text{-NiO-N (1:1)}$	-0.83	-0.22	0.60	86	2.24	0.46	177	1.09	0.1 M KOH	This work
$\text{Ni/Mn}_2\text{O}_3\text{-NiO-N (1:2)}$	-1.21	-0.32	0.60	100	3.17	0.48	169	1.11	0.1 M KOH	This work
$\text{Ni/Mn}_2\text{O}_3\text{-NiO-N (2:1)}$	-1.18	-0.29	0.65	87	3.97	0.54	176	1.12	0.1 M KOH	This work
$\text{PtNi/Mn}_2\text{O}_3\text{-NiO-N (1:1)}$	-1.64	-0.45	0.65	129	3.82	0.53	146	1.11	0.1 M KOH	This work
$\text{PtNi/Mn}_2\text{O}_3\text{-NiO-N (1:2)}$	-2.94	-1.37	0.77	67	3.38	0.50	156	0.96	0.1 M KOH	This work
$\text{PtNi/Mn}_2\text{O}_3\text{-NiO-N (2:1)}$	-2.93	-1.28	0.70	67	3.52	0.50	143	1.03	0.1 M KOH	This work
$\text{FeCo@N-HC}$	-5.80	-	0.85	97	3.98	0.32	92	0.70	0.1 M KOH	[15]
$\text{NiFeCoNC}$	-6.00	-	0.84	-	4.00	0.36	-	0.75	0.1 M KOH	[16]
$\text{LaMnNiCoO}_3 (1:2:3)$	-5.90	-	0.75	80	3.99	0.37	-	0.85	0.1 M KOH	[17]

Table 2. Cont.

Material	ORR Parameters					OER Parameters		$\Delta E$ */V	Electrolyte	Source
	$j_d$ /mA cm <sup>-2</sup>	$j_k$ /mA cm <sup>-2</sup>	$E_{1/2}$ /V	b/mV dec <sup>-1</sup>	n	$\eta_{10}$ /V	b/mV dec <sup>-1</sup>			
Ni <sub>0.33</sub> Co <sub>0.67</sub> O <sub>x</sub>	-5.80	-	0.81	-	3.89	0.28	76	0.70	0.1 M KOH	[18]
MnFe <sub>2</sub> O <sub>4</sub>	-4.70	-	0.71	71	3.88	0.58	-	1.10	0.1 M KOH	[51]
NiFe <sub>2</sub> O <sub>4</sub>	-4.95	-	0.68	57	3.76	0.41	-	0.96	0.1 M KOH	[51]
NiO-Mn <sub>2</sub> O <sub>3</sub> -CDs	-6.00	-	0.84	126	3.85	0.30	141	0.69	0.1 M KOH	[52]
Pt/Mn <sub>2</sub> O <sub>3</sub> -NiO	-4.48	-4.34	0.79	62 and 109	3.73	0.54	154	0.98	0.1 M KOH	[19]
PtNi/Mn <sub>2</sub> O <sub>3</sub> -NiO	-4.32	-3.10	0.79	63 and 103	3.99	0.53	140	0.97	0.1 M KOH	[19]
IrO <sub>2</sub>	-	-	-	-	-	0.36	84	-	0.1 M KOH	[53]
RuO <sub>2</sub>	-	-	-	-	-	0.40	-	-	0.1 M KOH	[16]
Pt/C (40 wt.%)	-6.44	14.90	0.86	79 and 60	3.97	0.58	198	0.95	0.1 M KOH	[19]

HC—honeycomb carbon; CDs—carbon dots. \*  $\Delta E$  represents estimation for cases where diffusion-limited current density was not reached.

### 3.6. EIS and Stability Study of Tested Electrocatalysts

Electrochemical impedance spectroscopy, EIS, was used to gain deeper insight into the origin of resistance in the electrochemical system used herein to test the synthesized catalysts.

Nyquist plots are presented in Figure 11, in which the high-frequency intersection with the  $Z'$ -axis represents the sum of all the electrolyte resistances, electrode material, and wiring,  $R_s$ . Charge-transfer resistance,  $R_{ct}$ , was calculated as the low-frequency intersection with the  $Z'$ -axis from which  $R_s$  was subtracted. Furthermore, it should be mentioned that the flattening of the semicircles in Nyquist plots indicates dispersive capacitance [54]. The  $R_s$  values for all materials are almost identical (Table 3), showing consistency in the experiments, with a slight difference attributed to the change in cell geometry when the working electrode is replaced. The lowest value of charge-transfer resistance was calculated for Ni-decorated materials, which was expected since Ni and its oxides are well-known for OER catalysis [55,56]. The highest values of  $R_{ct}$  were calculated for N-doped BMOs and N-doped BMOs decorated with Pt. PtNi-decorated materials show slightly higher  $R_{ct}$  values than Ni-decorated ones, supporting their good OER performance.

Figure 12 presents the results of a stability study for the two best-performing electrocatalysts, Pt/Mn<sub>2</sub>O<sub>3</sub>-NiO-N and PtNi/Mn<sub>2</sub>O<sub>3</sub>-NiO-N, with a BMO-to-N ratio of 1:2. Both the studied materials showed good stability under ORR conditions, with the PtNi-decorated N-doped BMO showing more consistent current density throughout the 4 h experiment, as shown in Figure 12a. Pt-decorated material showed a slight drop in current density during the last 30 min of the test, indicating a slight degradation of its catalytic performance, which is not the case with PtNi-decorated material. During the “switch test”, alternating between ORR and OER modes, the PtNi-decorated N-doped BMO showed good stability and superior bifunctional performance compared with Pt/Mn<sub>2</sub>O<sub>3</sub>-NiO-N, as seen in Figure 12b,c. For Pt/Mn<sub>2</sub>O<sub>3</sub>-NiO-N (1:2), the OER current density drops to 0 mA cm<sup>-2</sup> after only 1 h into the experiment; in contrast, although PtNi/Mn<sub>2</sub>O<sub>3</sub>-NiO-N (1:2) shows a current drop, it still retains a measurable current density even after 10 h testing. The low stability of Pt electrocatalysts and thus of the Pt/Mn<sub>2</sub>O<sub>3</sub>-NiO-N (1:2) studied herein can be attributed to the aggregation of the Pt nanoparticles due to Ostwald ripening [57,58]. Conversely, the boosted performance, activity, as well as stability of PtNi/Mn<sub>2</sub>O<sub>3</sub>-NiO-N (1:2) can be attributed to both the electronic effect of the presence of the second metal, i.e., modification of the Pt binding energy, and geometric effect, i.e., reduction in Pt-Pt bond length [58].

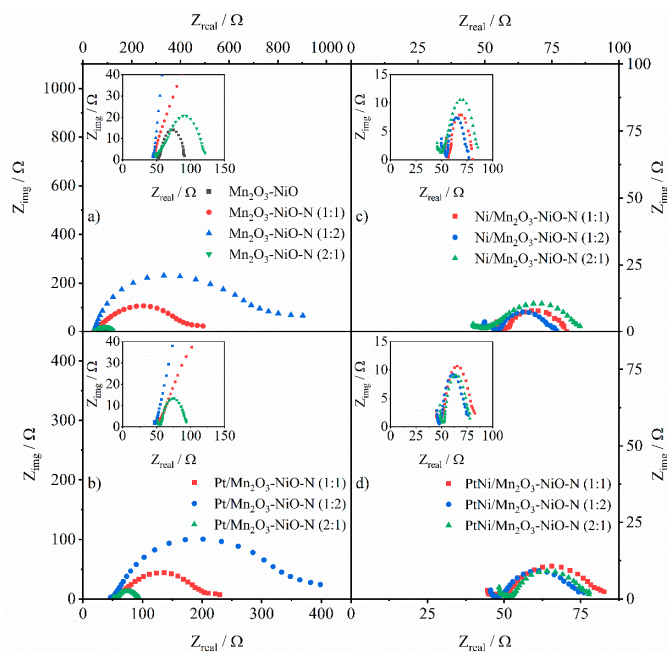


**Figure 11.** EIS analysis at 1.8 V of (a) pure and N-doped  $\text{Mn}_2\text{O}_3\text{-NiO}$ , (b) Pt-decorated N-doped  $\text{Mn}_2\text{O}_3\text{-NiO}$ , (c) Ni-decorated N-doped  $\text{Mn}_2\text{O}_3\text{-NiO}$ , and (d) PtNi-decorated N-doped  $\text{Mn}_2\text{O}_3\text{-NiO}$ .

**Table 3.** Comparison of EIS analysis parameters for the synthesized BMO-based electrocatalysts.

Material	$R_s/\Omega$	$R_{ct}/\Omega$
$\text{Mn}_2\text{O}_3\text{-NiO}$	52.6	38.3
$\text{Mn}_2\text{O}_3\text{-NiO-N (1:1)}$	45.7	380
$\text{Mn}_2\text{O}_3\text{-NiO-N (1:2)}$	45.1	710
$\text{Mn}_2\text{O}_3\text{-NiO-N (2:1)}$	49.0	71.0
Pt/ $\text{Mn}_2\text{O}_3\text{-NiO-N (1:1)}$	53.0	144
Pt/ $\text{Mn}_2\text{O}_3\text{-NiO-N (1:2)}$	47.5	306
Pt/ $\text{Mn}_2\text{O}_3\text{-NiO-N (2:1)}$	55.5	38.5
Ni/ $\text{Mn}_2\text{O}_3\text{-NiO-N (1:1)}$	56.1	24.4
Ni/ $\text{Mn}_2\text{O}_3\text{-NiO-N (1:2)}$	54.6	22.1
Ni/ $\text{Mn}_2\text{O}_3\text{-NiO-N (2:1)}$	50.0	35.4
PtNi/ $\text{Mn}_2\text{O}_3\text{-NiO-N (1:1)}$	48.5	32.2
PtNi/ $\text{Mn}_2\text{O}_3\text{-NiO-N (1:2)}$	47.6	27.5
PtNi/ $\text{Mn}_2\text{O}_3\text{-NiO-N (2:1)}$	51.8	25.5

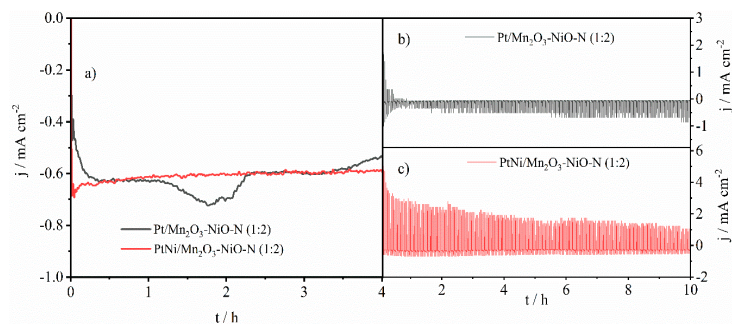


**Figure 12.** (a) ORR stability study for Pt/ $\text{Mn}_2\text{O}_3\text{-NiO-N (1:2)}$  and PtNi/ $\text{Mn}_2\text{O}_3\text{-NiO-N (1:2)}$ , and “switch test” for (b) Pt/ $\text{Mn}_2\text{O}_3\text{-NiO-N (1:2)}$  and (c) PtNi/ $\text{Mn}_2\text{O}_3\text{-NiO-N (1:2)}$ .

#### 4. Conclusions

This study systematically evaluates the bifunctional ORR/OER performance of electrocatalysts containing Pt and Ni nanoparticles on nitrogen-doped mixed metal oxide supports in an alkaline medium. The electrocatalysts were successfully synthesized by microwave irradiation as a simple and time-saving technique. The synthesized catalysts were characterized using physicochemical and electrochemical analysis methods. It was determined that the results obtained from physicochemical characterization are compatible with each other and with the literature data. PtNi/Mn<sub>2</sub>O<sub>3</sub>-NiO-N with a BMO-to-N ratio of 1:2 demonstrated the best performance regarding bifunctional electrochemical activity and stability among the studied materials.

Namely, the best catalytic performance towards ORR was shown by PtNi/Mn<sub>2</sub>O<sub>3</sub>-NiO (2:1), PtNi/Mn<sub>2</sub>O<sub>3</sub>-NiO (1:1), and PtNi/Mn<sub>2</sub>O<sub>3</sub>-NiO (1: 2) with their limiting diffusion current densities at 1800 rpm in the range of  $-4.32$  to  $-4.81$  mA cm<sup>-2</sup> and a number of exchanged electrons of ca. 4, suggesting that oxygen reduction took place by a kinetically more favorable 4e<sup>-</sup> mechanism. PtNi/Mn<sub>2</sub>O<sub>3</sub>-NiO-N (2:1) and PtNi/Mn<sub>2</sub>O<sub>3</sub>-NiO-N (1:2) showed the lowest Tafel slope value of 67 mV dec<sup>-1</sup>. Regarding OER, three PtNi-based catalysts again showed the lowest Tafel slopes (143–156 mV dec<sup>-1</sup>) among all the catalysts tested herein. The lowest  $\Delta E$  value of 0.96 V was determined for PtNi/Mn<sub>2</sub>O<sub>3</sub>-NiO-N (1:2), which was slightly higher than that of Pt/Mn<sub>2</sub>O<sub>3</sub>-NiO-N (2:1) (0.88 V), which contains ca. double the amount of Pt compared to the PtNi catalyst (~20 wt.% Pt for Pt catalysts and ~10 wt.% Pt for PtNi catalysts). Finally, the good bifunctional performance of the PtNi/Mn<sub>2</sub>O<sub>3</sub>-NiO-N (1:2) electrocatalyst was confirmed by a stability test simulating operation in a real fuel cell with the smallest current drop.

**Supplementary Materials:** The following supporting information can be downloaded at: <https://www.mdpi.com/article/10.3390/pr12030453/s1>, Physical characterization; Electrochemical measurements.

**Author Contributions:** Conceptualization, B.Š., D.M.F.S., Š.M. and A.B.Y.; investigation, D.M., Y.A. and G.S.P.S.; formal analysis, D.M. and Y.A.; writing—original draft preparation, D.M., Y.A. and G.S.P.S.; writing—review and editing, B.Š., D.M.F.S., Š.M., A.B.Y. and G.S.P.S.; visualization, D.M. and Y.A.; supervision, B.Š., D.M.F.S., Š.M. and A.B.Y. All authors have read and agreed to the published version of the manuscript.

**Funding:** The authors would like to thank the Ministry of Science, Technological Development and Innovation of the Republic of Serbia (contract no. 451-03-65/2024-03/200146 and 451-03-66/2024-03/200146), as well as Fundação para a Ciência e a Tecnologia, Portugal, for a research contract in the scope of programmatic funding UIDP/04540/2020 (D.M.F. Santos) and contract no. IST-ID/156-2018 (B. Šljukić).

**Data Availability Statement:** Data are available on request to the corresponding author.

**Conflicts of Interest:** The authors declare no conflicts of interest. The funding bodies had no role in the design of the study; in the collection, analyses, or interpretation of data; in the writing of the manuscript, and in the decision to publish the results.

#### References

1. Available online: <https://www.theworldcounts.com> (accessed on 9 October 2023).
2. Utz, R.C.; Teledyne Energy Systems, Inc. *Study of Unitized Regenerative Fuel Cell Systems for Aircraft Applications*; Federal Aviation Administration. William J. Hughes Technical Center: Egg Harbor Township, NJ, USA, 2022. [CrossRef]
3. Ball, M.; Weeda, M. The hydrogen economy—Vision or reality? *Int. J. Hydrogen Energy* **2015**, *40*, 7903–7919. [CrossRef]
4. Crabtree, G.W.; Dresselhaus, M.S.; Buchanan, M.V. The hydrogen economy. *Phys. Today* **2004**, *57*, 39–44. [CrossRef]
5. Barreto, L.; Makihiro, A.; Riahi, K. The hydrogen economy in the 21st century: A sustainable development scenario. *Int. J. Hydrogen Energy* **2003**, *28*, 267–284. [CrossRef]
6. Wang, Y.; Leung, D.Y.C.; Xuan, J.; Wang, H. A review on unitized regenerative fuel cell technologies, part B: Unitized regenerative alkaline fuel cell, solid oxide fuel cell, and microfluidic fuel cell. *Renew. Sustain. Energy Rev.* **2017**, *75*, 775–795. [CrossRef]

7. Sadhasivam, T.; Dhanabalan, K.; Roh, S.H.; Kim, T.H.; Park, K.W.; Jung, S.; Kurkuri, M.D.; Jung, H.Y. A comprehensive review on unitized regenerative fuel cells: Crucial challenges and developments. *Int. J. Hydrogen Energy* **2017**, *42*, 4415–4433. [[CrossRef](#)]
8. Ge, X.; Sumboja, A.; Wu, D.; An, T.; Li, B.; Goh, F.W.T.; Hor, T.S.A.; Zong, Y.; Liu, Z. Oxygen reduction in alkaline media: From mechanisms to recent advances of catalysts. *ACS Catal.* **2015**, *5*, 4643–4667. [[CrossRef](#)]
9. Adzic, R. *Recent Advances in the Kinetics of Oxygen Reduction*; Brookhaven National Laboratory: Upton, NY, USA, 1996. [[CrossRef](#)]
10. Miles, M.H.; Klaus, E.A.; Gunn, B.P.; Locker, J.R.; Serafin, W.E.; Srinivasan, S. The oxygen evolution reaction on platinum, iridium, ruthenium and their alloys at 80 °C in acid solutions. *Electrochim. Acta* **1978**, *23*, 521–526. [[CrossRef](#)]
11. Wen, X.; Bai, L.; Li, M.; Guan, J. Ultrafine iridium oxide supported on carbon nanotubes for efficient catalysis of oxygen evolution and oxygen reduction reactions. *Mater. Today Energy* **2018**, *10*, 153–160. [[CrossRef](#)]
12. Song, F.; Bai, L.; Moysiadou, A.; Lee, S.; Hu, C.; Liardet, L.; Hu, X. Transition metal oxides as electrocatalysts for the oxygen evolution reaction in alkaline solutions: An application-inspired renaissance. *J. Am. Chem. Soc.* **2018**, *140*, 7748–7759. [[CrossRef](#)] [[PubMed](#)]
13. Goswami, C.; Hazarika, K.K.; Bharali, P. Transition metal oxide nanocatalysts for oxygen reduction reaction. *Mater. Sci. Energy Technol.* **2018**, *1*, 117–128. [[CrossRef](#)]
14. Yuan, C.; Wu, H.B.; Xie, Y.; Lou, X.W. Mixed transition-metal oxides: Design, synthesis, and energy-related applications. *Angew. Chem.—Int. Ed.* **2014**, *53*, 1488–1504. [[CrossRef](#)]
15. Han, Z.; Lin, S.Y.; Feng, J.J.; Zhang, L.; Zhang, Q.L.; Wang, A.J. Transitional metal alloyed nanoparticles entrapped into the highly porous N-doped 3D honeycombed carbon: A high-efficiency bifunctional oxygen electrocatalyst for boosting rechargeable Zn-air batteries. *Int. J. Hydrogen Energy* **2021**, *46*, 19385–19396. [[CrossRef](#)]
16. Kisand, K.; Sarapuu, A.; Kikas, A.; Kisand, V.; Rähn, M.; Treshchalov, A.; Käärik, M.; Piirsoo, H.M.; Aruväli, J.; Paiste, P.; et al. Bifunctional multi-metallic nitrogen-doped nanocarbon catalysts derived from 5-methylresorcinol. *Electrochem. Commun.* **2021**, *124*, 106932. [[CrossRef](#)]
17. Sun, J.; Du, L.; Sun, B.; Han, G.; Ma, Y.; Wang, J.; Huo, H.; Zuo, P.; Du, C.; Yin, G. A bifunctional perovskite oxide catalyst: The triggered oxygen reduction/evolution electrocatalysis by moderated Mn-Ni co-doping. *J. Energy Chem.* **2021**, *54*, 217–224. [[CrossRef](#)]
18. Xue, Y.; Ma, G.; Wang, X.; Jin, M.; Akinoglu, E.M.; Luo, D.; Shui, L. Bimetallic hollow tubular NiCoO<sub>x</sub> as a bifunctional electrocatalyst for enhanced oxygen reduction and evolution reaction. *ACS Appl. Mater. Interfaces* **2021**, *13*, 7334–7342. [[CrossRef](#)]
19. Mladenović, D.; Santos, D.M.F.; Bozkurt, G.; Soyulu, G.S.P.; Yurtcan, A.B.; Miljanić, Š.; Šljukić, B. Tailoring metal-oxide-supported PtNi as bifunctional catalysts of superior activity and stability for unitised regenerative fuel cell applications. *Electrochem. Commun.* **2021**, *124*, 106963. [[CrossRef](#)]
20. Kotta, A.; Ansari, S.A.; Parveen, N.; Fouad, H.; Alothman, O.Y.; Khaled, U.; Seo, H.K.; Ansari, S.G.; Ansari, Z.A. Mechanochemical synthesis of melamine doped TiO<sub>2</sub> nanoparticles for dye sensitized solar cells application. *J. Mater. Sci. Mater. Electron.* **2018**, *29*, 9108–9116. [[CrossRef](#)]
21. Li, W.; Zhao, D. An overview of the synthesis of ordered mesoporous materials. *Chem. Commun.* **2013**, *49*, 943–946. [[CrossRef](#)] [[PubMed](#)]
22. Yao, L.; Liu, Q.; Mossin, S.; Nielsen, D.; Kong, M.; Jiang, L.; Yang, J.; Ren, S.; Wen, J. Promotional effects of nitrogen doping on catalytic performance over manganese-containing semi-coke catalysts for the NH<sub>3</sub>-SCR at low temperatures. *J. Hazard. Mater.* **2020**, *387*, 121704. [[CrossRef](#)] [[PubMed](#)]
23. Aykut, Y.; Yurtcan, A.B. Catalyst development for viability of electrochemical hydrogen purifier and compressor (EHPC) technology. *Int. J. Hydrogen Energy* **2022**, *47*, 19619–19632. [[CrossRef](#)]
24. Mladenović, D.; Daş, E.; Santos, D.M.F.; Yurtcan, A.B.; Šljukić, B. Highly efficient oxygen electrode obtained by sequential deposition of transition metal-platinum alloys on graphene nanoplatelets. *Materials* **2023**, *16*, 3388. [[CrossRef](#)]
25. Luan, V.H.; Tien, H.N.; Hur, S.H.; Han, J.H.; Lee, W. Three-dimensional porous nitrogen-doped NiO nanostructures as highly sensitive NO<sub>2</sub> sensors. *Nanomaterials* **2017**, *7*, 313. [[CrossRef](#)]
26. Ievtushenko, A.; Khyzhun, O.; Shteplyuk, I.; Tkach, V.; Lazorenko, V.; Lashkarev, G. X-ray photoelectron spectroscopy study of nitrogen and aluminum-nitrogen doped ZnO films. *Acta Phys. Pol. A* **2013**, *124*, 858–861. [[CrossRef](#)]
27. Cui, Y.; Zhang, J.; Zhang, G.; Huang, J.; Liu, P.; Antonietti, M.; Wang, X. Synthesis of bulk and nanoporous carbon nitride polymers from ammonium thiocyanate for photocatalytic hydrogen evolution. *J. Mater. Chem.* **2011**, *21*, 13032–13039. [[CrossRef](#)]
28. Yang, G.; Yan, W.; Wang, J.; Yang, H. Fabrication and formation mechanism of Mn<sub>2</sub>O<sub>3</sub> hollow nanofibers by single-spinneret electrospinning. *CrystEngComm* **2014**, *16*, 6907–6913. [[CrossRef](#)]
29. Taghizadeh, F. The study of structural and magnetic properties of NiO nanoparticles. *Opt. Photonics J.* **2016**, *6*, 164–169. [[CrossRef](#)]
30. Abel, M.J.; Pramothkumar, A.; Archana, V.; Senthilkumar, N.; Jothivenkatachalam, K.; Prince, J.J. Facile synthesis of solar light active spinel nickel manganite (NiMn<sub>2</sub>O<sub>4</sub>) by co-precipitation route for photocatalytic application. *Res. Chem. Intermed.* **2020**, *46*, 3509–3525. [[CrossRef](#)]
31. Liu, Z.; Hong, L.; Tham, M.P.; Lim, T.H.; Jiang, H. Nanostructured Pt/C and Pd/C catalysts for direct formic acid fuel cells. *J. Power Sources* **2006**, *161*, 831–835. [[CrossRef](#)]

32. Tientong, J.; Garcia, S.; Thurber, C.R.; Golden, T.D. Synthesis of nickel and nickel hydroxide nanopowders by simplified chemical reduction. *J. Nanotechnol.* **2014**, *2014*, 193162. [[CrossRef](#)]
33. Mathis, T.S.; Kurra, N.; Wang, X.; Pinto, D.; Simon, P.; Gogotsi, Y. Energy storage data reporting in perspective—Guidelines for interpreting the performance of electrochemical energy storage systems. *Adv. Energy Mater.* **2019**, *9*, 1902007. [[CrossRef](#)]
34. Marković, N.M.; Schmidt, T.J.; Stamenković, V.; Ross, P.N. Oxygen reduction reaction on Pt and Pt bimetallic surfaces: A selective review. *Fuel Cells* **2001**, *1*, 105–116. [[CrossRef](#)]
35. Nørskov, J.K.; Rossmeisl, J.; Logadottir, A.; Lindqvist, L.; Kitchin, J.R.; Bligaard, T.; Jónsson, H. Origin of the overpotential for oxygen reduction at a fuel-cell cathode. *J. Phys. Chem. B* **2004**, *108*, 17886–17892. [[CrossRef](#)]
36. Shao, M.H.; Liu, P.; Adzic, R.R. Superoxide anion is the intermediate in the oxygen reduction reaction on platinum electrodes. *J. Am. Chem. Soc.* **2006**, *128*, 7408–7409. [[CrossRef](#)] [[PubMed](#)]
37. Ma, R.; Lin, G.; Zhou, Y.; Liu, Q.; Zhang, T.; Shan, G.; Yang, M.; Wang, J. A review of oxygen reduction mechanisms for metal-free carbon-based electrocatalysts. *NPJ Comput. Mater.* **2019**, *5*, 78. [[CrossRef](#)]
38. Masa, J.; Batchelor-McAuley, C.; Schuhmann, W.; Compton, R.G. Koutecky-Levich analysis applied to nanoparticle modified rotating disk electrodes: Electrocatalysis or misinterpretation. *Nano Res.* **2014**, *7*, 71–78. [[CrossRef](#)]
39. Li, D.; Batchelor-McAuley, C.; Compton, R.G. Some thoughts about reporting the electrocatalytic performance of nanomaterials. *Appl. Mater. Today* **2020**, *18*, 100404. [[CrossRef](#)]
40. Sokolov, S.V.; Sepunaru, L.; Compton, R.G. Taking cues from nature: Hemoglobin catalysed oxygen reduction. *Appl. Mater. Today* **2017**, *7*, 82–90. [[CrossRef](#)]
41. Mladenović, D.; Vujković, M.; Mentus, S.; Santos, D.M.F.; Rocha, R.P.; Sequeira, C.A.C.; Figueiredo, J.L.; Šljukić, B. Carbon-supported Mo<sub>2</sub>C for oxygen reduction reaction electrocatalysis. *Nanomaterials* **2020**, *10*, 1805. [[CrossRef](#)]
42. Shinagawa, T.; Garcia-Esparza, A.T.; Takanabe, K. Insight on Tafel slopes from a microkinetic analysis of aqueous electrocatalysis for energy conversion. *Sci. Rep.* **2015**, *5*, 13801. [[CrossRef](#)]
43. Chen, M.; Liu, J.; Zhou, W.; Lin, J.; Shen, Z. Nitrogen-doped graphene-supported transition-metals carbide electrocatalysts for oxygen reduction reaction. *Sci. Rep.* **2015**, *5*, 10389. [[CrossRef](#)]
44. Milikić, J.; Vasić, M.; Amaral, L.; Cvjetičanin, N.; Jugović, D.; Hercigonja, R.; Šljukić, B. NiA and NiX zeolites as bifunctional electrocatalysts for water splitting in alkaline media. *Int. J. Hydrogen Energy* **2018**, *43*, 18977–18991. [[CrossRef](#)]
45. Retuerto, M.; Calle-Vallejo, F.; Pascual, L.; Ferrer, P.; García, Á.; Torrero, J.; Gianolio, D.; Fierro, J.L.G.; Peña, M.A.; Alonso, J.A. Role of lattice oxygen content and Ni geometry in the oxygen evolution activity of the Ba-Ni-O system. *J. Power Sources* **2018**, *404*, 56–63. [[CrossRef](#)]
46. Menezes, P.W.; Panda, C.; Loos, S.; Bunschei-Bruns, F.; Walter, C.; Schwarze, M.; Deng, X.; Dau, H.; Driess, M. A structurally versatile nickel phosphite acting as a robust bifunctional electrocatalyst for overall water splitting. *Energy Environ. Sci.* **2018**, *11*, 1287–1298. [[CrossRef](#)]
47. Kumar, J.P.; Giri, S.D.; Sarkar, A. Mesoporous NiO with different morphology: Synthesis, characterization and their evaluation for oxygen evolution reaction. *Int. J. Hydrogen Energy* **2018**, *43*, 15639–15649. [[CrossRef](#)]
48. Da Zhang, W.; Hu, Q.T.; Wang, L.L.; Gao, J.; Zhu, H.Y.; Yan, X.; Gu, Z.G. In-situ generated Ni-MOF/LDH hetero-structures with abundant phase interfaces for enhanced oxygen evolution reaction. *Appl. Catal. B* **2021**, *286*, 119906. [[CrossRef](#)]
49. Fang, L.; Niu, S.; Wang, S.; Lu, Y.; Cheng, Y. Enhanced oxygen reduction catalytic performance of PtNi alloy through modulating metal-support interaction. *Appl. Catal. A Gen.* **2024**, *669*, 119511. [[CrossRef](#)]
50. Hyun, K.; Lee, J.H.; Yoon, C.W.; Cho, Y.H.; Kim, L.H.; Kwon, Y. Improvement in oxygen reduction activity of polypyrrole-coated PtNi alloy catalyst prepared for proton exchange membrane fuel cells. *Synth. Met.* **2014**, *190*, 48–55. [[CrossRef](#)]
51. Si, C.; Zhang, Y.; Zhang, C.; Gao, H.; Ma, W.; Lv, L.; Zhang, Z. Mesoporous nanostructured spinel-type MFe<sub>2</sub>O<sub>4</sub> (M = Co, Mn, Ni) oxides as efficient bi-functional electrocatalysts towards oxygen reduction and oxygen evolution. *Electrochim. Acta* **2017**, *245*, 829–838. [[CrossRef](#)]
52. Shao, C.; Liao, F.; Zhu, W.; Zhang, Y.; Ma, M.; Yang, J.; Yin, K.; Shao, M.; Jiang, B. Carbon dots bridge NiO and Mn<sub>2</sub>O<sub>3</sub> as highly efficient bifunctional oxygen electrocatalysts for rechargeable zinc-air batteries. *Appl. Surf. Sci.* **2022**, *596*, 153642. [[CrossRef](#)]
53. Paul, A.; Silva, T.A.R.; Soliman, M.M.A.; Karačić, J.; Šljukić, B.; Alegria, E.C.B.A.; Khan, R.A.; da Silva, M.F.C.G.; Pombeiro, A.J.L. Benzimidazole Schiff base copper (II) complexes as catalysts for environmental and energy applications: VOC oxidation, oxygen reduction and water splitting reactions. *Int. J. Hydrogen Energy* **2022**, *47*, 23175–23190. [[CrossRef](#)]
54. Swierk, J.R.; Klaus, S.; Trotochaud, L.; Bell, A.T.; Tilley, T.D. Electrochemical study of the energetics of the oxygen evolution reaction at nickel iron (oxy)hydroxide catalysts. *J. Phys. Chem. C* **2015**, *119*, 19022–19029. [[CrossRef](#)]
55. Vij, V.; Sultan, S.; Harzandi, A.M.; Meena, A.; Tiwari, J.N.; Lee, W.G.; Yoon, T.; Kim, K.S. Nickel-based electrocatalysts for energy-related applications: Oxygen reduction, oxygen evolution, and hydrogen evolution reactions. *ACS Catal.* **2017**, *7*, 7196–7225. [[CrossRef](#)]
56. Nadesan, J.C.B.; Tseung, A.C.C. Oxygen evolution on nickel oxide electrodes. *J. Electrochem. Soc.* **1985**, *132*, 2957–2959. [[CrossRef](#)]

57. Martins, M.; Milikić, J.; Šljukić, B.; Soyly, G.S.P.; Yurtcan, A.B.; Bozkurt, G.; Santos, D.M.F. Mn<sub>2</sub>O<sub>3</sub>-MO (MO = ZrO<sub>2</sub>; V<sub>2</sub>O<sub>5</sub>, WO<sub>3</sub>) supported PtNi nanoparticles: Designing stable and efficient electrocatalysts for oxygen reduction and borohydride oxidation. *Microporous Mesoporous Mater.* **2019**, *273*, 286–293. [[CrossRef](#)]
58. Guo, D.J.; Cui, S.K.; Cheng, D.; Zhang, P.; Jiang, L.; Zhang, C.C. One-pot synthesis of PtNi alloy nanoflowers supported on multi-walled carbon nanotubes with superior electrocatalytic activity for the oxygen reduction. *J. Power Sources* **2014**, *255*, 157–162. [[CrossRef](#)]

**Disclaimer/Publisher's Note:** The statements, opinions and data contained in all publications are solely those of the individual author(s) and contributor(s) and not of MDPI and/or the editor(s). MDPI and/or the editor(s) disclaim responsibility for any injury to people or property resulting from any ideas, methods, instructions or products referred to in the content.